



Unraveling the Origins of Gamma-Ray Burst X-Ray Plateaus through a Study of X-Ray Flares

H. Dereli-Bégué¹ , A. Pe'er¹ , D. Bégué¹ , and F. Ryde² ¹ Department of Physics, Bar-Ilan University, Ramat-Gan 52900, Israel² Department of Physics, KTH Royal Institute of Technology and The Oskar Klein Centre, SE-106 91 Stockholm, Sweden

Received 2024 December 15; revised 2025 April 3; accepted 2025 April 19; published 2025 May 29

Abstract

The X-ray light curves of gamma-ray bursts (GRBs) display complex features, including plateaus and flares, that challenge theoretical models. Here, we study the properties of flares that are observed in the early afterglow phase (up to a few thousand seconds). We split the sample into two groups: bursts with and without an X-ray plateau. We find that the distributions of flare properties are similar in each group; specifically, the peak time (t_{pk}) of the flares and the ratio of the flare width to the flare peak time (w/t_{pk}), which is found to be ≈ 1 , regardless of the presence of a plateau. We discuss these results in view of the different theoretical models aimed at explaining the origin of the plateau. These results are difficult to explain by viewing angle effects or late-time energy injection, but do not contradict the idea that GRBs with X-ray plateaus have a low Lorentz factor, on the order of tens. For these GRBs, the dissipation processes that produce the flares naturally occur at smaller radii compared to GRBs with higher Lorentz factors, while the flares maintain a similar behavior. Our results therefore provide independent support for the idea that many GRBs have a Lorentz factor of a few tens rather than a few hundreds.

Unified Astronomy Thesaurus concepts: Gamma-ray bursts (629); Light curves (918); Astronomy data analysis (1858); Relativistic jets (1390); Non-thermal radiation sources (1119)

1. Introduction

Gamma-ray bursts (GRBs) are extremely energetic events and are known to have highly relativistic jets, with initial expansion Lorentz factors typically ranging from tens to thousands (J. H. Krolik & E. A. Pier 1991; E. E. Fenimore et al. 1993; J. L. Racusin et al. 2011; H. Dereli-Bégué et al. 2022). GRBs display two sequential phases: the prompt emission phase, followed by the afterglow phase. These two phases can be explained within the framework of the classical GRB fireball model (M. J. Rees & P. Meszaros 1992; P. Mészáros et al. 1998; T. Piran 2004; P. Mészáros 2006; P. Kumar & B. Zhang 2015) where the GRB prompt gamma-ray emission is caused by internal energy dissipation (e.g., shocks) within a collimated ultrarelativistic jet, and the broadband afterglow emission is created by an external shock propagating into the circumburst medium, which can be either a stellar wind or a constant-density interstellar medium (ISM; P. Meszaros & M. J. Rees 1997; R. Sari et al. 1998).

Following the launch of the Neil Gehrels Swift Observatory (hereafter Swift; N. Gehrels et al. 2004), several previously unknown features in the X-ray light curves have been observed. Notably, while the late-time X-ray emission (after $\sim 10^{3.5} - 10^4$ s), aligns with the theoretical predictions of the classical fireball model, other phenomena such as early steep decays, X-ray plateaus, and X-ray flares observed by Swift do not fit as straightforwardly within this model (J. A. Nousek et al. 2006; P. T. O’Brien et al. 2006; B. Zhang et al. 2006; P. A. Evans et al. 2007, 2009).

The early steep decay, characterized by a temporal index between $3 \leq \alpha \leq 5$, is associated with the end of the prompt

phase and is attributed to high-latitude emission arising from photons emitted at larger angles relative to the jet axis (corresponding to the observer direction), leading to a rapid decline in observed intensity (S. D. Barthelmy et al. 2005; G. Tagliaferri et al. 2005; R. Willingale et al. 2007; S. Ronchini et al. 2021). The following X-ray plateaus, with a shallow temporal index between $0 \leq \alpha \leq 0.7$, generally appear $100 - 10^3$ s after the GRB trigger and are usually followed by a late-time “afterglow” decay with an index between $1.2 \leq \alpha \leq 1.5$ (B. Zhang et al. 2006; H. Dereli-Bégué et al. 2022), as is expected theoretically (P. Meszaros & M. J. Rees 1993). Therefore, the flux during the plateau phase decreases slower than theoretically expected. This feature is observed in a substantial fraction, close to 60% of all GRBs (P. A. Evans et al. 2009; M. G. Dainotti et al. 2010, 2017; G. P. Srinivasaragavan et al. 2020, and references therein).

Since its discovery in early 2005, several ideas have been proposed to explain the X-ray plateau phase. It was initially proposed that the origin of the plateau phase is a continuous energy injection into the external shock from the central compact object, which produces the energy powering the GRB. This central engine can either be a newly formed black hole (B. Zhang et al. 2006; J. Granot & P. Kumar 2006; J. A. Nousek et al. 2006; L. Li et al. 2018) or a millisecond magnetar (S. Dall’Osso et al. 2011; B. D. Metzger et al. 2011; A. Rowlinson et al. 2014; N. Rea et al. 2015; G. Stratta et al. 2018; S. Ronchini et al. 2023). In order to overcome an energy crisis that occurs in this scenario, it was further suggested that the microphysical parameters may vary in time (R. Hascoët et al. 2014). Moreover, it was argued that continuous energy injection would affect the dynamics of the reverse shock, which could result in a plateau signal and could explain the origin of the observed correlations (H. van Eerten 2014; H. J. van Eerten 2014). Moreover, a few studies have interpreted the plateau phase within the framework of accretion onto a black hole (P. Kumar et al. 2008a, 2008b;



Original content from this work may be used under the terms of the [Creative Commons Attribution 4.0 licence](https://creativecommons.org/licenses/by/4.0/). Any further distribution of this work must maintain attribution to the author(s) and the title of the work, journal citation and DOI.

J. K. Cannizzo et al. 2011). However, these models do not fully address the physical origin of the observed correlations. Recently, A. Ł. Lenart et al. (2025) proposed a model in which the plateau phase arises from energy extraction via black hole spin-down in a magnetically arrested disk. This model aims to explain various observational features, including the plateau luminosity–time anticorrelation.

Alternatively, it was suggested that the observed plateau is due to viewing angle effects, where structured jets are observed slightly off-axis (D. Eichler & J. Granot 2006; K. Toma et al. 2006; D. Eichler 2014; P. Beniamini et al. 2020a, 2020b; G. Oganessian et al. 2020). Recently, we suggested a different explanation, according to which the observed signal originates from an outflow that is observed on axis, but reaches a maximum Lorentz factor of several tens at most, expanding into a medium composed of a low-density wind (R. Shen & C. D. Matzner 2012; H. Dereli-Bégué et al. 2022). It is therefore of interest to find an observational measure that could discriminate between these models.

X-ray flares typically peak between 100–10⁵ s after the prompt emission and are observed in about half of the GRB population, mostly in long GRBs but rarely in short GRBs (D. N. Burrows et al. 2005; G. Chincarini et al. 2007, 2010; A. D. Falcone et al. 2007; P. A. Curran et al. 2008; M. G. Bernardini et al. 2011; R. Margutti et al. 2011). They usually appear as one or two flares, with cases of multiple flares being rare (e.g., M. Perri et al. 2007; A. A. Abdo et al. 2011; J. Saji et al. 2023). Flares can be considerably energetic and are often characterized by large flux variations (A. D. Falcone et al. 2006; S. L. Gibson et al. 2018). Indeed, their fluence can be up to 100% of the prompt fluence, and the flare fluxes, measured with respect to the underlying continuum, $\Delta F_{\text{flare}}/F_{\text{cont.}}$, can vary over short timescales $\Delta t/t_{\text{pk}} \lesssim 1$ where Δt measures the duration of the flare and t_{pk} is the time of maximum flare flux with respect to the trigger time (G. Chincarini et al. 2007). Since flares share many properties with the prompt emission, it is widely accepted that they are powered by the late central engine activities either by internal shocks (Y. Z. Fan & D. M. Wei 2005; K. Ioka et al. 2005; B. Zhang et al. 2006), or some other dissipation process within the ultrarelativistic outflow (D. Giannios 2006; D. Lazzati et al. 2011), but at later times and at lower energies.

Since flares are so abundant, they are observed both in GRBs with and without plateaus. Given that different theoretical models about the origin of the plateau phase have different expectations about the observed properties of flares, comparing flare properties in GRBs with and without plateaus can potentially be used as an independent way of discriminating between the different models. The only study we are aware of to date is that of S.-X. Yi et al. (2022), who compared the X-ray flare energy and the X-ray plateau energy with the isotropic prompt emission energy and found that all are correlated. We note however that their method to obtain afterglow and flare properties is not fully self-consistent as they take their values from studies which separately study these properties. Here, we conduct a comprehensive study on the properties of flares observed in Swift GRBs with and without plateaus. We then discuss the implications for the different theoretical models.

This paper is organized as follows. In Section 2, we define the data collection and analysis method, with sample selection and model definition as well as the fitting procedure and best

model selection. In Section 3, we present the flare analysis results. In Section 4, we then discuss how our definition of flares could impact the results. In Section 5, we discuss the physical interpenetration of the results. Finally, in Section 6, we list our summary and conclusions. Throughout the paper, a flat Lambda cold dark matter (Λ CDM) cosmological model with cosmological parameters $\Omega_m = 0.286$ and $H_0 = 70 \text{ km s}^{-1} \text{ Mpc}^{-1}$ are used (G. Hinshaw et al. 2009).

2. Data Collection and Analysis Method

2.1. Sample Selection

We selected a statistically significant sample of 100 GRBs by antichronologically searching through 8 yr of data from the Swift archive, starting 2022 December 2. As for our first paper on this topic (H. Dereli-Bégué et al. 2022), the selection criteria are as follow. First, the redshift of the burst has to be measured by spectroscopy. We note that recent studies demonstrated that machine learning methods can provide redshift estimates for GRBs without spectroscopic measurements (M. G. Dainotti et al. 2024; A. Narendra et al. 2024). While these advancements are promising and could potentially increase the sample size and improve the statistical robustness of GRB studies, they have not been incorporated in this work. The second criterion limits the sample to those GRBs which triggered the Swift Burst Alert Telescope (Swift-BAT). Indeed, GRBs that are not observed by BAT usually lack Swift X-Ray Telescope (Swift-XRT) observations, preventing us from performing the fitting procedure described in the following sections. In fact, even GRBs initially detected by Swift-BAT can lack a sufficiently large number of data points, and those GRBs were removed from the sample. Although gaps in the Swift-XRT light curves could be addressed by reconstructing the light curve as demonstrated in M. G. Dainotti et al. (2023), we have not applied such a method in this study. Instead, we require the number of data points to be ≥ 5 at the beginning or end of each independent decaying feature, e.g., plateau, late afterglow decay, etc. These phases were identified in the light curve presented in the Swift online repository.

2.2. Model Definition

GRB afterglow light curves are made of several components, namely (i) the early afterglow steep decay; (ii) the plateau (when it exists); (iii) the late-time afterglow (“the self-similar decay”) slope; and (iv) the post-jet-break decay. On top of these, there are (v) flares (when they exist). Combining all components lead to the so-called canonical X-ray light curve (J. A. Nousek et al. 2006; P. T. O’Brien et al. 2006; B. Zhang et al. 2006). Yet each component can be observed independently of the others, creating the rich afterglow phenomena, and providing a unique challenge in fitting and interpreting the afterglow light curves.

To investigate both flare and plateau properties, our analysis method is as follows. In our approach, we model the light curve using continuous power-law segments that can have either one, two, three, or four segments. Flares are modeled using the “Norris” function (J. P. Norris et al. 2005). They are integrally part of the models and their properties are constrained during the fit, alongside those of the underlying afterglow. For full details of the fitting procedure, see Section 2.3 and Appendix A below.

The difficulty in handling multicomponent models, considering for instance several flares, the underlying afterglow emission, and eventually a jet break, is due to the large number of parameters and the resulting high model flexibility, which allows the “naive” model to fit any light curve at the expense of a physical interpretation. A solution to this problem is to prescribe conditions that are simultaneously sufficiently general for the model to accurately represent the data or clearly fail when attempting to do so, while also being sufficiently physically motivated to obtain meaningful and interpretable results.

Here, we choose to fit each X-ray light curve, starting from the “steep decay” phase (when it exists). Following the steep decay, we apply a physically motivated afterglow model, based on synchrotron emission from particles accelerated by the propagating forward shock wave, assuming spherical symmetry. The shock-accelerated electrons assume a power-law distribution, with power-law index p , in between Lorentz factors γ_{\min} and γ_{\max} . This leads to two relevant characteristic frequencies in the observed spectra, ν_m , which is the typical emission frequency from electrons at γ_{\min} , and ν_c , which is the cooling frequency. As was shown by several authors (e.g., J. Granot & R. Sari 2002; H. Dereli-Bégué et al. 2022), various combinations of light curves and spectra can be obtained. The resulting light curve depends on (i) the evolutionary stage of the blast wave propagation—coasting versus self-similar decaying phase; (ii) the ambient medium profile—stellar wind or constant-density ISM; and (iii) the observed frequency, which can be smaller, larger, or in between ν_m and ν_c .

In addition to the above mentioned possibilities, when fitting the light curves, we add three additional categories: (i) a steep decay is fitted as a power law in time, with a slope that is independent on the electron power-law index and steeper than two; (ii) inclusion of a jet break; and (iii) a number of flares, which we consider to vary between zero, one, or two. Combined together, we consider a total of 36 different models used in fitting the data. Although the models we use assume spherical symmetry, we point out that deviation from spherical symmetry predictions is expected at late times (after the jet break), while all the flares identified occur at much earlier times, before the jet break. Therefore, the key properties of the flares we are interested in (peak time and flare width) are only weakly sensitive to this assumption. For a complete description of the models used, see Appendix A.

In our analysis, flares take the shape of the Norris function (J. P. Norris et al. 2005; G. Chincarini et al. 2010):

$$\mathcal{N}(T) = A_f \lambda \exp \left[-\frac{\tau_1}{T - t_0} - \frac{T - t_0}{\tau_2} \right], \quad (1)$$

if $T > t_0$ and $\mathcal{N}(T) = 0$ otherwise. Here, A_f is the flare amplitude, t_0 is the onset time of the flare, τ_1 and τ_2 are, respectively, two flare shape parameters related to the rise and decay phases altering the flare profile and in particular its asymmetry, and $\lambda = \exp(2\mu)$ where $\mu = (\tau_1/\tau_2)^{1/2}$. The maximum of the flare is reached at time $t_{\text{pk}} = t_0 + (\tau_1\tau_2)^{1/2}$ and its maximum equals to $\mathcal{N}(t_{\text{pk}}) = A_f$. The factor A_f quantifies the relative enhancement of the flux due to the flare. Following G. Chincarini et al. (2010) and noting that we fit the logarithm of the flux, one can define the flare flux

variability as

$$\frac{\Delta F_{\text{flare}}}{F_{\text{cont.}}} = \frac{10^{\mathcal{N}(t_{\text{pk}})} 10^{F_{\text{cont.}}} - 10^{F_{\text{cont.}}}}{10^{F_{\text{cont.}}}} = 10^{\mathcal{N}(t_{\text{pk}})} - 1, \quad (2)$$

where F_{flare} and $F_{\text{cont.}}$ are the flare and underlying afterglow fluxes, respectively.

An important property of X-ray flares is their temporal aspect ratio w/t_{pk} , where w is the temporal width of the flare. Flare width has been estimated in various ways and using different functions, including, e.g., a symmetric Gaussian (G. Chincarini et al. 2007), a smoothly broken power-law profile (S.-X. Yi et al. 2016), and using the Norris function (J. P. Norris et al. 2005). For the latter, G. Chincarini et al. (2010) and M. G. Bernardini et al. (2011) define the flare width w as the time interval during which the contribution of the flare is larger than $1/e$ of its maximum, leading to $w = \Delta t_{1/e} = \tau_2(1 + 4\mu)^{1/2}$. We cannot use this definition directly, since the fits are performed in log space. Instead, we determine the times \bar{t}_1 and $\bar{t}_2 > \bar{t}_1$,³ between which the Norris function has value at least half of its maximum. The width is then define as

$$w = 10^{\bar{t}_2} - 10^{\bar{t}_1}. \quad (3)$$

Furthermore, it is important to note that different definitions of flare widths can lead to variations in absolute width measurements. For instance, the FWHM may provide a narrower estimate compared to widths calculated at lower thresholds, such as 5% of the maximum flux. However, the overall characterization of w/t_{pk} remains consistent across these definitions. Defining w at 5% of the maximum captures a broader interval around the peak than the FWHM, while still providing a similar interpretation in temporal analyses, particularly when comparing the relative timescales of flares.

Moreover, while the choice of model—such as the asymmetric Norris profile (J. P. Norris et al. 2005)—may produce different width measurements compared to symmetric Gaussian profiles (G. Chincarini et al. 2007), these alternative definitions do not substantially affect the theoretical interpretations of physical processes. Thus, although definitions differ, the temporal ratio w/t_{pk} provides a robust measure across various models, allowing for a consistent interpretation of flare variability and duration using different methods. A detailed, quantitative discussion on the definition of a flare and the calculation of w/t_{pk} appear in Section 4 below.

The isotropic-equivalent energy $E_{\text{iso},f}$ emitted in each flare can be calculated once the fit is performed. We calculate it using

$$E_{\text{iso},f} = 4\pi d_L^2 \cdot C_F \cdot \int_{\bar{t}_1}^{\bar{t}_2} 10^{F_{\text{cont.}}} (10^{\mathcal{N}(T)} - 1) \times 10^T \ln(10) dT. \quad (4)$$

Here, d_L is the luminosity distance and C_F is a flux conversion factor, which converts count rate to flux (obtained from the online Swift repository). The integral represents the total count rate of the flare between \bar{t}_1 and \bar{t}_2 . We point out that the total energy is not sensitive to the exact choice of the integration boundaries, as the flux rises and decays exponentially.

Finally, for comparison with previous studies (e.g., J. P. Norris et al. 2005; G. Chincarini et al. 2010), we define

³ We note these times \bar{t} to avoid confusion with the break time of the afterglow T_1 , T_2 , and T_3 .

Table 1
Parameters Used in the Fitting Procedure

Parameter	Units	Minimum	Maximum	Type of Distribution
T_1	s	xdata(min)	4	Logarithmic
T_2	s	0.5	3	Logarithmic
T_3	s	0.5	3	Logarithmic
A	...	-10	10	Linear
b	...	-5	-2	Linear
p	...	2	3	Linear
q	...	0	1.5	Linear
t_1	s	xdata(min) - 0.1	3.5	Logarithmic
A_{f1}	...	0.2	3	Linear
$\tau_{1,1}$	s	-2.1	-0.2	Logarithmic
$\tau_{1,2}$	s	-2.1	-0.2	Logarithmic
t_2	s	0.2	2	Logarithmic
A_{f2}	...	0.2	3	Linear
$\tau_{2,1}$	s	-2.1	-0.2	Logarithmic
$\tau_{2,2}$	s	-2.1	-0.2	Logarithmic

Note. For each parameter we include its units, prior allowed ranges, and the sampling distribution. The parameters are divided into two parts. The top part includes the parameters of the underlying afterglow: T_1 , T_2 , and T_3 represent the break times; A is the normalization; b is the slope of the steep decay; p is the electron power-law index; and q , together with p , defines the slope of the decay phase after the jet break (see Appendix A). The bottom part includes the parameters of the flares when present: t_1 and t_2 are the start times of the flares; A_{f1} and A_{f2} are the flare amplitudes; and $\tau_{1,1}$, $\tau_{1,2}$, $\tau_{2,1}$, and $\tau_{2,2}$ are the rise and decay time parameters that shape the flare profiles.

the flare asymmetry as

$$k = (1 + 4\mu)^{-1/2}. \quad (5)$$

2.3. Fitting Procedure

The X-ray count rate light curves (hereinafter LCs) of each GRB have been downloaded from the online Swift repository⁴ (P. A. Evans et al. 2007, 2009), considering the full Swift-XRT bandpass, i.e., $(E_{\min}, E_{\max}) = (0.3, 10)$ keV. We then fit each individual LC with all 36 considered models, all described in Section 2.2 and Appendix A. Although the LCs could have been sorted into categories in order to reduce the number of models per LC, we decided against this to avoid introducing human bias into the analysis process and best model selection.

To perform the fit, we assume a Gaussian likelihood and sample the posterior distributions with MultiNest (F. Feroz et al. 2009), a nested sampling algorithm designed for efficient Bayesian inference. We assume 8000 (1000 for the model without flares) active points and a tolerance of 0.5 to ensure efficient sampling and convergence. MultiNest offers a number of advantages, including computational efficiency and the ability to robustly handle multimodal posterior distributions, which is a relevant possibility given the high dimensionality and complexity of the parameter space for the models we considered, specifically for those with one or two flares. MultiNest also computes the evidence, which is the key to perform model comparison, see Section 2.4.

The parameter ranges and their sampling distributions, either uniform or log uniform, are summarized in Table 1. For example, the electron power-law index p is sampled linearly from a noninformative uniform prior within the range of 2–3,

similar to the parameters A , b , q , A_{f1} , and A_{f2} as seen in Table 1. Parameters related to time i.e., T_1 , T_2 , and T_3 as well as the rise and decay time parameter for the Norris function for the flares follow log-uniform priors to account for their wide range and scale sensitivity.

In our analysis, for the flare amplitude, we set a minimum value of 0.2 for A_{f1} and A_{f2} , corresponding to an increase by a factor of 1.58 for the flare flux relative to the underlying continuum in the linear scale. This ensures that the flare flux is always at least 1.58 times larger than the underlying continuum flux, allowing for clear identification of flares and preventing the misidentification of small random flux variations in the LC as flares.

2.4. Best Model Selection and Verification

Our best model selection is based on Bayesian model comparison methods and the following strategy. The first step is to discard cases where there is a lack of data near the peak time of the flare. One of the challenges in analyzing GRB X-ray data is the lack of observations, specifically on the timescale of a few thousand seconds, corresponding to the orbit time of Swift (e.g., Earth occultation), which can significantly affect the accuracy of the model fitting. To address this, we incorporate a criterion that considers the density of data points around the peak time of each flare. Specifically, if there are fewer than two data points within the time interval from the start to the peak of the flare, the model is flagged as unreliable and the model is discarded from further consideration. Indeed, this situation arises when a single or two data points within the full LC can be better explained by a very narrow flare. In fact, this criterion ensures that the model has sufficient data to accurately characterize the rise, the peak and the decay of the flare.

In the next step, we aim to balance the complexity of the model with its ability to fit the data well. This is achieved by prioritizing models with fewer parameters, provided they adequately capture the observed phenomena. The potential best models are identified for each case (C/F and E for wind or H and G for ISM, see Appendix A for details on the nomenclature) by comparing nested models one by one based on the Bayes factor and excluding those with a Bayes factor larger than 5. This process ensures that only models with balanced performance and fewer parameters advance to the next stage. While this initial selection narrows down the models effectively, the Bayes factor is not always well suited for nonnested model comparisons, as prior choices can heavily influence the Bayes factor. To address this limitation, we adopt the Akaike information criterion (AIC) as an additional criterion. AIC and the corrected AIC (AICc) provide a consistent framework for comparing nonnested models. Therefore, among all potential models, the best model is selected based on the lowest AICc value, as AICc accounts for potential overfitting and bias, particularly in models with small sample sizes. If AICc is unavailable, the model with the lowest AIC is chosen instead. Finally, the residuals between the model and the data are computed for each selected model and visually inspected to ensure that it does not exhibit outliers—namely data points with residuals significantly different from the others—or systematic deviations, which are consistent patterns of misfit. Once the fit is finished and the analysis performed, we exclude 11 GRBs from the remaining of the analysis, as in these GRBs flares were misidentified, resulting

⁴ https://www.swift.ac.uk/xrt_curves/

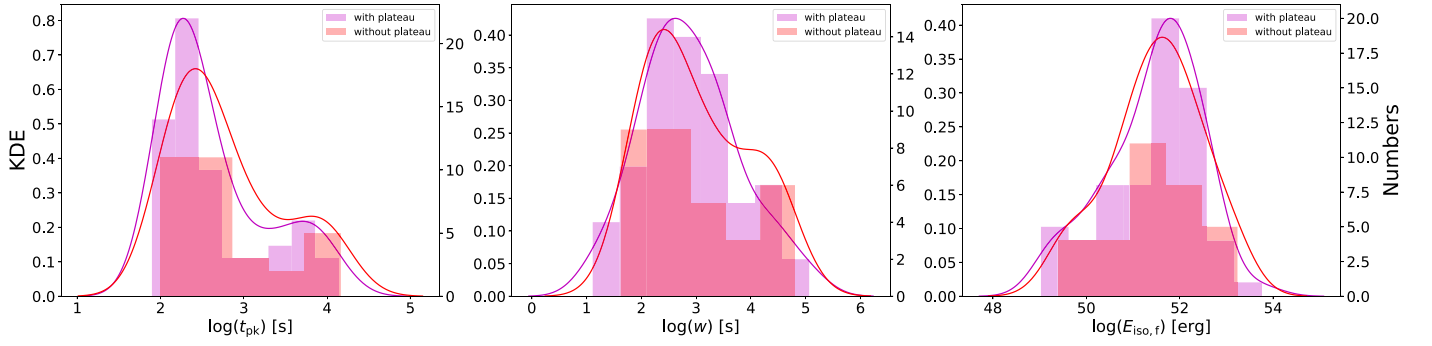


Figure 1. Distributions of the flare peak time, t_{pk} (left), the flare width w (middle), and the flare isotropic energy, $E_{\text{iso},f}$ (right). The 65 flares obtained from the 42 bursts with a plateau phase are in purple, while the 32 flares obtained from the 19 GRBs without a plateau phase are in red. In each panel, the right-hand ordinate shows the number of bursts in each bin while the left-hand ordinate shows the value of the kernel density estimation (KDE) drawn by the purple and red solid lines. These distributions show that the properties of the flare are independent of the presence of a plateau phase in the GRB X-ray LCs.

in failures of the different afterglow models to adequately fit the data. A detailed description of the reasoning for excluding these 11 GRBs is provided in Appendix B.

3. Flare Analysis Results

From the remaining 89 bursts in our sample, we find the following.

- (i) Sixty-one bursts (69% of GRBs in our sample) have flares. This indicates that flares are quite common in GRB afterglows. This value is slightly higher than previously reported, where about half of the GRBs were found to exhibit flares (B. Zhang et al. 2006; G. Chincarini et al. 2010).
- (ii) Fifty-seven GRBs in our sample (64%) have an X-ray plateau.
- (iii) Among the 61 GRBs with flares, 42 (68%) have a plateau, while 19 bursts do not.
- (iv) Of the 57 GRBs that have a plateau, 42 (73%) also exhibit flares.

These results imply that the overall occurrence of flares in GRBs without a plateau phase (19/32 = 59%) is not statistically differ from the occurrence of flares in GRBs with a plateau phase (42/57 = 73%). This strongly suggests that the presence of flares is independent of the existence of a plateau, indicating that these two phenomena, namely plateaus and flares, are most likely not related or dependent on each other.

Here, we focus on analyzing the properties of flares, and we therefore focus on the subsample of 61 GRBs with flares. A complete analysis of the afterglow properties of all GRBs in our sample will appear elsewhere (H. Dereli-Bégué et al. 2025, in preparation). The properties of all flares that appear in the 61 bursts in our sample are listed in Table C1 in Appendix C.

3.1. Flare Energetics, Time of Occurrence, and Duration

In order to study possible correlations between flare properties and the existence of a plateau, we split the flare sample into two. The first part contains 65 flares identified in the X-ray LCs of 42 bursts with a plateau phase, while the second part includes 32 flares identified in the LCs of 19 GRBs without a plateau phase. Figure 1 shows the distributions of the flare peak times t_{pk} , the flare width w , and the flare isotropic energy $E_{\text{iso},f}$. Flares that originate from bursts with a plateau are colored in purple, and those that are detected in GRBs without a plateau are in red. Comparing the averages, we find

that $\langle \log_{10} t_{\text{pk}} \rangle = 2.64 \pm 0.08$ for GRBs with a plateau, to be compared with $\langle \log_{10} t_{\text{pk}} \rangle = 2.79 \pm 0.11$ for bursts without a plateau. A similar result holds for the width w and the flare isotropic energy $E_{\text{iso},f}$, with $\langle \log_{10} w \rangle = 2.89 \pm 0.11$ and $\langle \log_{10} E_{\text{iso},f} \rangle = 51.43 \pm 0.12$ to be compared to $\langle \log_{10} w \rangle = 3.02 \pm 0.16$ and $\langle \log_{10} E_{\text{iso},f} \rangle = 51.49 \pm 0.17$ for bursts with and without a plateau, respectively. We further performed a Kolmogorov–Smirnov (K-S) test for each parameter and found that (i) the K-S test statistic is $D = 0.23$ with a probability $p = 0.18$ for t_{pk} ; (ii) $D = 0.11$ and $p = 0.92$ for the width; and (iii) $D = 0.10$ and $p = 0.96$ for $E_{\text{iso},f}$. Since $p > 0.05$, we cannot reject the null hypothesis at the 5% significance level; this suggests that the two subsamples originate from the same population. Additionally, a multivariate K-S test is performed for t_{pk} and width as they have similar scales (as opposed to, e.g., $E_{\text{iso},f}$, which has a very different scale), and are strongly correlated (see Figure 3). The test statistic was found to be $D = 0.24$ and $D_{\text{critical}} = 0.61$. Since $D < D_{\text{critical}}$, we do not find sufficient statistical evidence to reject the null hypothesis at the 5% significance level. Therefore, we conclude that the joint distributions of t_{pk} and width do not differ between the two subsamples, suggesting that they originate from the same population. This is consistent with the results of the one-dimensional K-S test for each individual variable.

We therefore conclude that the flares origin and properties are independent on the afterglow properties, which are determined by the ambient medium and forward shock properties. In particular, this means that flares are independent of the existence of a plateau phase. This conclusion is aligned with the conclusion of G. Chincarini et al. (2010), who similarly argued that flare properties are independent of the ambient medium (though plateaus were not considered in that work).

Furthermore, from Figure 1, we find that both subsamples show a heavy tail toward high flare peak times and widths. This may indicate a possible existence of two populations of flares, namely narrow and wide flares. We point out that the current statistics in this region of the parameter space is small. An analysis of the complete sample of bursts observed with Swift would allow to resolve this issue and firmly confirmed the existence of two kinds of flares.

In Figure 2, we present the distribution of the ratio of the flare width to the flare peak time w/t_{pk} and the distribution of the flare flux variability $\Delta F_{\text{flare}}/F_{\text{cont}}$. Comparing the averages, we find that $\langle \log_{10} w/t_{\text{pk}} \rangle = 0.25 \pm 0.07$ for GRBs with a plateau, to be compared with $\langle \log_{10} w/t_{\text{pk}} \rangle = 0.22 \pm 0.09$ for

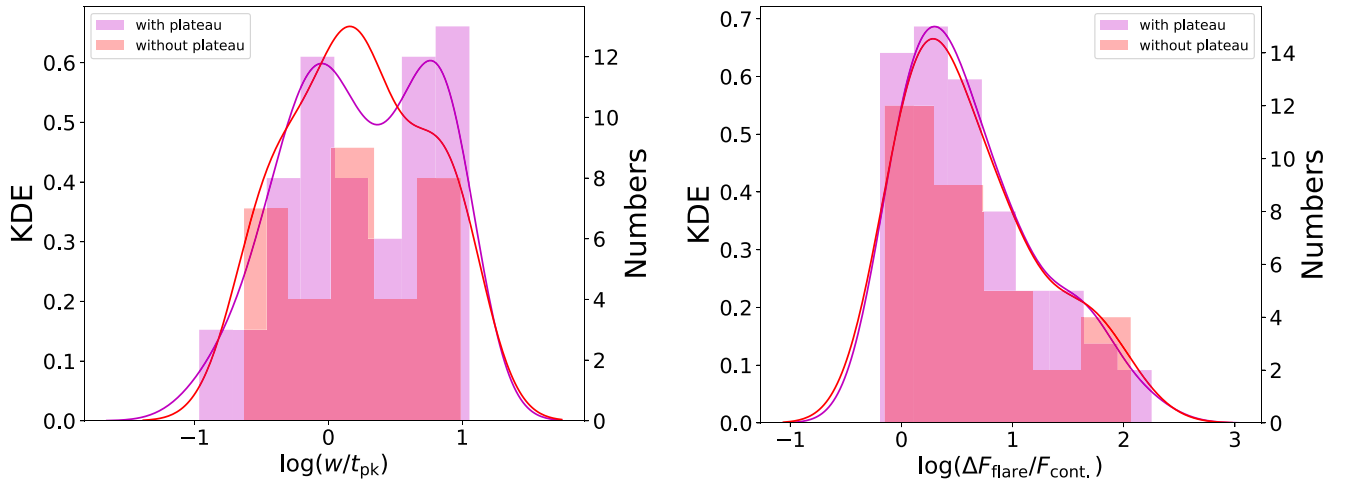


Figure 2. Distributions of the ratio of the flare width to the flare peak time, w/t_{pk} (left), and the flare flux variability, $\Delta F_{\text{flare}}/F_{\text{cont.}}$ (right). The data presentation, including the color coding, is the same as in Figure 1, where purple represents the 65 flares from 42 bursts with a plateau phase, and red represents the 32 flares from 19 GRBs without a plateau phase. The errors correspond to a significance of 1σ . The results show that the flare time and flux variability properties are the same, regardless of whether there is a plateau phase in the GRBs X-ray LCs. Additionally, bimodal distributions are observed in both subsamples in the distributions of the ratio of the flare width to the flare peak time. This bimodality is more pronounced for the GRBs with a plateau phase.

burst without a plateau. A similar result holds for the flux variability, $\langle \log_{10} \Delta F_{\text{flare}}/F_{\text{cont.}} \rangle = 0.63 \pm 0.07$ to be compared with $\langle \log_{10} \Delta F_{\text{flare}}/F_{\text{cont.}} \rangle = 0.63 \pm 0.11$ for bursts with and without a plateau, respectively. A K-S test for each parameter reveals $D = 0.12$ and $p = 0.88$ for w/t_{pk} , and $D = 0.08$ and $p = 0.99$ for $\Delta F_{\text{flare}}/F_{\text{cont.}}$. Similarly, with $p > 0.05$, the results support the null hypothesis, confirming that the two subsamples originate from the same population. An important result is that the ratio of the flare width to the flare peak time (w/t_{pk}) is ≈ 1 , regardless of the presence of a plateau.

Additional checks. In the analysis presented in this section, we considered all flares obtained from both the window timing (WT) mode and the photon counting (PC) mode of the Swift-XRT instrument, irrespective of the burst duration T_{90} . Therefore, the sample of flares might be contaminated by episodes of the prompt emission, namely the flares identified at early times in our analysis might be due to late prompt phase activity. To understand if these flares impact the results, we applied an additional criterion to the flare sample, considering only the flares characterized by $t_{pk} > T_{90}$, and repeated the analysis. This cut resulted in the exclusion of 11 flares for bursts with a plateau phase and four flares for bursts without a plateau phase. We found that the conclusions remain unchanged after applying this additional cut. In particular, we find that $\langle \log_{10} t_{pk} \rangle = 2.73 \pm 0.09$ for GRBs with a plateau, compared with $\langle \log_{10} t_{pk} \rangle = 2.86 \pm 0.12$ for bursts without a plateau.

In addition, it has been suggested that there may be a distinction between early ($t_{pk} < 1000$ s; as studied, e.g., by G. Chincarini et al. 2010; R. Duque et al. 2022) and late flares ($t_{pk} \geq 1000$ s; e.g., M. G. Bernardini et al. 2011). Considering this possibility as well, we limited the sample to flares for which $T_{90} < t_{pk} < 1000$ s to ensure that the flares are not contaminated by the prompt emission and occur at early times. As a result of these additional criteria, the sample size was significantly reduced, comprising 38 flares for GRBs with a plateau phase and 18 flares for GRBs without a plateau phase. Despite these stringent selection criteria and substantially reduced-sized sample, the ratio w/t_{pk} remains the same, enlightening the solidity of this result.

One last aspect to examine is the possible temporal evolution of the peak time of flares with increasing redshift (D. Kocevski & V. Petrosian 2013; M. G. Dainotti et al. 2017). When analyzing the redshift distribution (see Table C1) of the two subsamples (the K-S test statistic is $D = 0.16$ with a probability $p = 0.83$), we find no significant difference. Therefore, both samples are similarly affected by increasing redshift in the context of the temporal evolution of the flare peak time. This does not impact the results of our analysis presented above.

3.2. Correlations between Flare Parameters

The relation between the peak time t_{pk} and the width w of each X-ray flare is presented in Figure 3. The result of the Spearman's rank correlation coefficient $r = 0.68$ (0.77) with a corresponding chance probability of $p \ll 10^{-2}$ ($\ll 10^{-2}$) shows a strong positive correlation between the width w and the t_{pk} for both subsamples with and without a plateau, respectively. This indicates that the longer the peak time t_{pk} , the wider the flare. We performed a fit to the correlation using the functional form $t_{pk} = C \cdot w^r$, where C is a proportionality constant and r is the power-law index. To account for uncertainties, large errors in the data were capped at the median uncertainty value, reducing the impact of highly uncertain points. We found the power-law index $r = 0.87 \pm 4.2 \times 10^{-5}$ for burst with a plateau and $r = 0.97 \pm 5.9 \times 10^{-5}$ for bursts without a plateau.

This result is in agreement with the previous findings of G. Chincarini et al. (2007, 2010); M. G. Bernardini et al. (2011); S.-X. Yi et al. (2016), albeit, in our analysis we find that this correlation remains true for GRBs with and without a plateau, underlying once more that flares do not seem to be associated to the phenomena giving rise to the plateau. We note that G. Chincarini et al. (2007, 2010) interpreted this tight correlation between t_{pk} and width w as an indication that flares are somewhat different from prompt phase episodes, as they do not follow such a correlation.

One of the characterizing properties of a flare's temporal behavior is its asymmetry. There are two ways of displaying flare asymmetry, either by studying k given in Equation (5) or

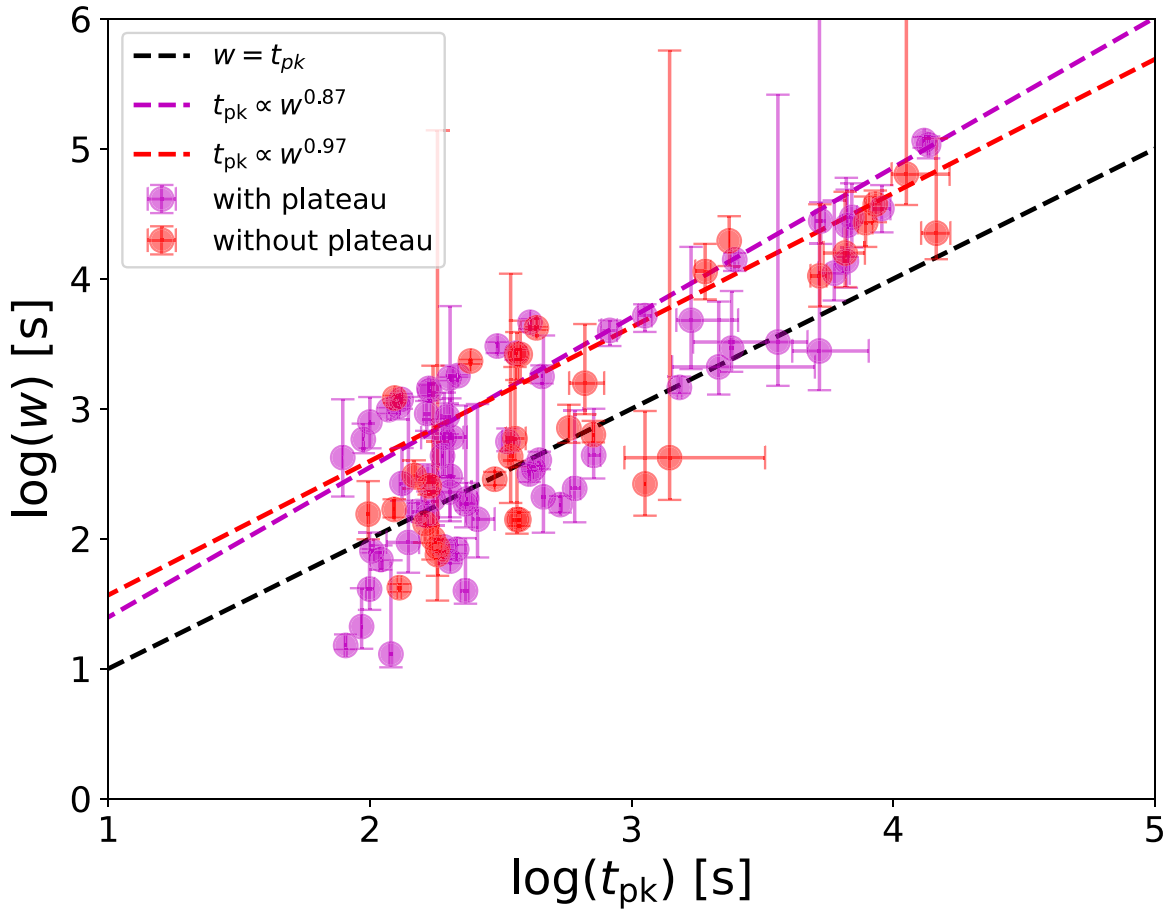


Figure 3. The relation between flare peak time (t_{pk}) and flare width (w). The purple points represent the 42 GRBs (65 flares) with a plateau phase, while the red points represent the 19 GRBs (32 flares) without a plateau phase in our subsamples. The Spearman’s rank correlation coefficient $r = 0.68$ (0.77), corresponding to a chance probability of $p \ll 10^{-2}$ ($\ll 10^{-2}$) indicates a strong monotonic relationship for GRBs with a plateau phase (without a plateau phase). To model the power-law relationship between t_{pk} and w , we performed a fit and find the power-law index to be $r = 0.87 \pm 4.2 \times 10^{-5}$ and $r = 0.97 \pm 5.9 \times 10^{-5}$ for GRBs with and without a plateau phase, respectively. The fitted relations are shown as dashed purple and red lines, respectively, matching the color coding of the data points. Additionally, the line of $w = t_{pk}$ is overlaid.

by analyzing the relation between t_{rise} and t_{decay} . In this work, we focus on the first option. In Figure 4, we find that the mean of k is 0.46 and 0.43 for both subsamples, with a standard deviation of 0.02. These values are consistent with those found in J. P. Norris et al. (2005) and G. Chincarini et al. (2010), where the median values are 0.49 and 0.35 with standard deviations of 0.26 and 0.2 for flares and prompt pulses, respectively.

4. Discussion: How to Define a Flare?

In our analysis, to identify a flare over the underlying continuum, we defined a minimum flare amplitude of 0.2 (corresponding to a factor of 1.58 in linear scale), which results in a flux cut. This is clearly visible in the flare flux variability distribution, $\Delta F_{flare}/F_{cont.}$, shown in Figure 2 (right). This approach naturally integrates the criteria for significant flare detection into the fitting process without the need for additional checks, providing a robust criterion for distinguishing significant flares from minor variations in the afterglow. While there is no universally accepted threshold in the literature, similar empirical criteria have been used in previous studies to identify significant flares. For instance, G. Chincarini et al. (2010) employed a combination of visual inspection and statistical analysis to identify flares in X-ray LCs, emphasizing the

importance of clear deviations from the afterglow model. Similarly, R. Margutti et al. (2011) utilized timing, duration, and flux increase criteria without specifying a strict numerical threshold, instead focusing on the statistical significance of the observed deviations. Our chosen threshold is consistent with these approaches, providing a balance between sensitivity to genuine flares and robustness against stochastic variations. By ensuring that detected flares exhibit a substantial increase in flux, our method aligns with the practices of A. D. Falcone et al. (2007), who required statistically significant increases in flux over the underlying afterglow. This threshold, therefore, offers a practical and validated approach to identifying significant flares in the context of our data and analysis framework.

Furthermore, in our analysis, we fit the data on a logarithmic scale, as opposed to the linear scale used in previous works. This approach provides several advantages. For instance, we identify one or two smoother flares in each LC, compared to previous studies that reported between one and seven or even more flares (A. D. Falcone et al. 2007; G. Chincarini et al. 2010). The resulting widths of the flares, as shown in Figure 1 (middle), appear broader than those previously reported by G. Chincarini et al. (2010), such as in GRB 051117A (see Figure 1 therein). Additionally, in Figure 2 (right), the flux variation $\Delta F_{flare}/F_{cont.}$ peaks at approximately five irrespective

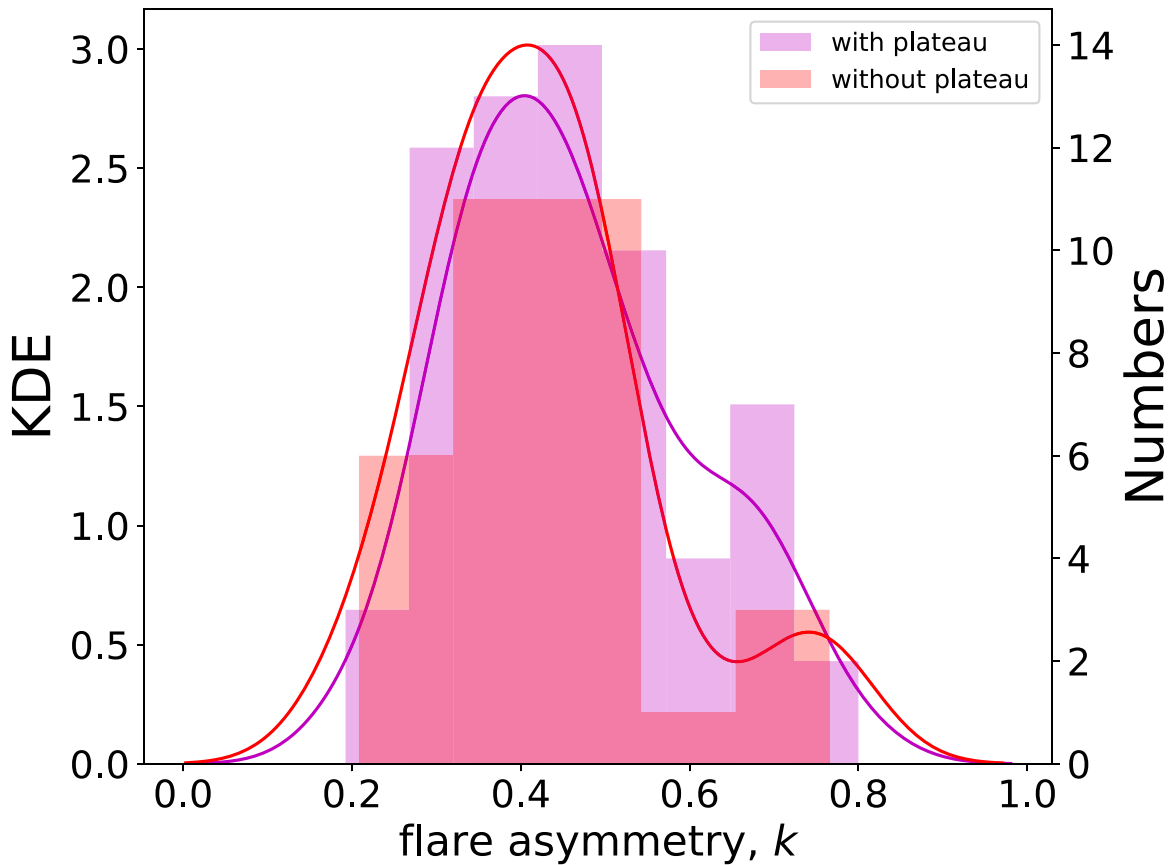


Figure 4. Distributions of the flare asymmetry, k . The purple bars represent the 42 GRBs (65 flares) with a plateau phase, while the red bars represent the 19 GRBs (32 flares) without a plateau phase. In each panel, the right-hand ordinate shows the number of burst in each histogram bin and the left-hand ordinate shows the value of the KDE, which are represented by the purple and red curves for each sample, respectively. We also performed K-S test for the flare asymmetry, k ($D = 0.21$ and $p = 0.23$).

of the environment, with a tail extending beyond 100. This result is consistent with the findings of G. Chincarini et al. (2010, see their Figure 13) and R. Margutti et al. (2011, see their Figure 7). The only difference is that the tail is shorter, not extending to 1000, and the second population is less clearly visible than in R. Margutti et al. (2011). This discrepancy might be due to our use of the logarithmic scaling.

Moreover, we calculate the ratio of the flare width to the flare peak time w/t_{pk} based on fits using an asymmetric model (J. P. Norris et al. 2005), following the approach of G. Chincarini et al. (2010). In this model, the width w is defined as the distance between two points where the function has dropped to 37% (or $1/e$) of its peak value. We find that the ratios of w/t_{pk} are approximately 0.25 ± 0.07 (1.78 linear scale) and 0.22 ± 0.09 (1.66 linear scale) for GRBs with and without a plateau, respectively (see Section 3.1). We find that our values are significantly larger than the 0.23 ± 0.14 reported by G. Chincarini et al. (2010), which was comparable to the 0.13 ± 0.10 result in G. Chincarini et al. (2007), where a narrower Gaussian fit was used under the assumption of symmetric flares.⁵ After converting to the Gaussian width at 37%, they found the width to be 2.83 times the Gaussian standard deviation (resulting in $w/t_{\text{pk}} = 0.28$). However, this is still lower than the values we obtain in our analysis.

⁵ In their analysis, the ratio of the flare width to the flare peak time was defined as Δ_i/t where Δ_i is the Gaussian width defined by $f = 0.05$, which refers to a specific point in time where the flux of a flare has decreased to 5% of its maximum value, and t is the Gaussian peak (G. Chincarini et al. 2007).

In contrast, our result is consistent with what D. Lazzati & R. Perna (2007) found. In their analysis, by assuming a spectral index $\beta \simeq 1$ they found $w/t_{\text{pk}} \sim 0.83$. This value aligns more closely with our findings of approximately 1.78 and 1.66 for GRBs with and without a plateau, respectively, although it still contrasts with the lower value of 0.23 ± 0.14 reported by G. Chincarini et al. (2010).

5. Physical Interpretation

By studying GRBs with flares and separating them into two subsamples, namely with or without a plateau phase, we found that the properties of the flares are independent of the existence of the plateau phase. This fact offers critical insights into the proposed emission models underlying the plateau phase.

The two key results we find are the following.

1. The flare peak time, t_{pk} , as seen in the Figure 1 (left), is on average the same for both subsamples, with and without a plateau phase.
2. Similarly, the ratio of the flare width to the flare peak time, as shown in Figure 2 (left), is approximately unity, irrespective of the existence of a plateau. As discussed in Section 3.1, removing possible prompt contamination or considering only early flares, do not change these results.

X-ray plateaus are ubiquitous in GRB X-ray LCs. Approximately 60% of GRBs exhibit this phase (P. A. Evans et al. 2009; G. P. Srinivasaragavan et al. 2020). This slower

than theoretically expected decline in flux in the early X-ray LC has challenged theoretical modeling for two decades now. Over the years, several models were suggested to explain this phenomenon. Here, we highlight some of the most discussed ones, and confront their predictions with the obtained results.

The first model suggested in the literature considers late-time continuous energy injection (J. Granot et al. 2006; J. A. Nousek et al. 2006; B. Zhang et al. 2006). This model explains the plateau phase by suggesting that late-time central engine activity provides energy that is injected into the decelerating external shock. This additional energy slows down the deceleration of the shock, hence the decay of the LC. The plateau ends when this energy injection ceases (Y. Fan & T. Piran 2006; J. Granot & P. Kumar 2006; J. Granot et al. 2006; B. Zhang et al. 2006; B. D. Metzger et al. 2011). This model successfully predicts achromatic breaks across X-ray and optical bands for certain bursts, such as GRB 060729 (D. Grupe et al. 2007). However, it struggles to account for chromatic afterglows, where X-ray and optical LCs do not show simultaneous breaks (J. A. Nousek et al. 2006). Extensions of this model, such as the introduction of two-component jets (J. L. Racusin et al. 2008) or reverse shock contributions (F. Genet et al. 2007; Z. L. Uhm & A. M. Beloborodov 2007), offer solutions but introduce additional complexities and parameters, making it challenging to fully interpret the variability observed in GRB behaviors (A. Panaitescu & P. Kumar 2001, 2002; S. A. Yost et al. 2003). One of the challenging issues with this model is the energy crisis; however, a few other models such as the energy injection effect on the reverse shock dynamics (H. van Eerten 2014; H. J. van Eerten 2014) or the modification of microphysical parameters (R. Hascoët et al. 2014) try to overcome this issue by using different properties of the energy injection. Yet, these models do not provide any predictions for the flare properties, unlike the others.

In addition, these energy injection model predictions conflict with our key findings. Late-time central engine activity may lead to the production of some late-time flares. In this case, one would expect that for GRBs with a plateau, the average flare occurrence time may be later than for GRBs without late energy injection (i.e., without a plateau). Alternatively, the average ratio of the flare width to its peak time, (w/t_{pk}) is expected to be lower if the energy injection that leads to the flare occurs at later times, as the flares will have a shorter time to develop and spread. Both these predictions are in contradiction with both of our key findings. The fact that t_{pk} is the same for both subsamples suggests it is not delayed central engine activity that produces the flares. The constant ratio ($w/t_{\text{pk}} \approx 1$) is a strong indication of a similar motion, such as internal expansion of shells that is proportional to the radius, and which originated at early times (during, or close to the observed prompt phase).

An alternative idea for explaining the plateau is that the observer is located off the jet axis (viewing angle effect), initially suggested by D. Eichler & J. Granot (2006). As was shown by several authors (K. Toma et al. 2006; D. Eichler 2014), an observer that is located slightly off the jet axis will observe an X-ray plateau, provided that the jet is structured (e.g., has an angle-dependent Lorentz factor). As the jet decelerates, progressively brighter material closer to the core becomes visible, leading to the shallow flux evolution observed during the plateau phase (P. Beniamini & E. Nakar 2019; P. Beniamini et al. 2020a). This model successfully predicts the plateau duration and flux as functions

of the jet structure and the observer’s viewing angle, establishing correlations between these properties and the GRB’s prompt emission characteristics (P. Beniamini et al. 2020a). However, while this model can account for achromatic plateaus in some bursts, it struggles to explain chromatic afterglows (D. Eichler & J. Granot 2006; G. Oganessian et al. 2020).

This model was recently extended to explain X-ray flares as delayed, deboosted versions of gamma-ray pulses produced in the jet’s core, while the plateau phase is interpreted as deboosted afterglow emission from the core (P. Beniamini et al. 2020b). In this scenario, energy dissipation that leads to flares would occur, on average, at the same radius, R for different GRBs. Different observers will observe the flares at different times, since the observed time is given by $t \sim R/\mathcal{D}^2c$, where \mathcal{D} is the Doppler boost, which is angle dependent. Therefore, it is expected that GRBs with plateaus would show flares occurring at later times. However, this expectation is contradicted by our finding in point (1), where the flare peak time, t_{pk} , is on average the same for GRBs with and without a plateau. Additionally, R. Duque et al. (2022) discuss that the off-axis interpretation can only account for a subset of observed flares, particularly those seen earlier, at $\lesssim 1000$ s. However, as discussed in Section 3.1, considering early flares did not affect the result in point (1). Moreover, the consistent patterns and similarity in flare characteristics, such as width, flare asymmetry, and variability relative to the continuum, suggest that the viewing angle might not significantly influence the observed properties.

A third model that was recently suggested is that the plateau originates from emission that occurs during the coasting phase of the propagating forward shock (R. Shen & C. D. Matzner 2012; H. Dereli-Bégué et al. 2022). This phase precedes the self-similar decaying phase that produces the late-time afterglow. As was shown by H. Dereli-Bégué et al. (2022), this model can naturally account for both the X-ray and optical signals without requiring complex modifications or additional parameters beyond the standard GRB “fireball” model framework. Its key difference than the classical GRB “fireball” evolution, is the assumption that during the coasting phase, the GRB Lorentz factor does not exceeds a few tens (rather than the common assumption of Lorentz factor of a few hundreds). Furthermore, this model requires that the explosion occurs in a low-density stellar wind environment, as is indeed expected for massive star GRB progenitors. This model effectively explains the plateau phase as due to synchrotron radiation from particles accelerated by the forward shock during the coasting phase.

This model provides several testable predictions. These include (1) the expectation that bursts with long plateau phases should not exhibit high-energy (GeV) emission or strong thermal components⁶ and (2) both chromatic and achromatic breaks are expected, resulting from the fact that different observed frequencies may be below or above the characteristic synchrotron cooling break (see H. Dereli-Bégué et al. 2022, for details).

The results found here are consistent with the predictions of this model. For GRBs with a lower Lorentz factor, energy dissipation processes producing the flares, such as, e.g.,

⁶ GRBs classified as Class II in H. Dereli-Bégué et al. (2022) have long and flat plateaus and do not show GeV emissions. Additionally, their variability time Δt_{min} is expected to be >5 . For example, GRBs classified as Class III may have a short and decaying plateau and might exhibit GeV emission.

collisions, are expected to occur at smaller radii compared to GRBs with a high Lorentz factor. For example, internal collisions originating from internal variability of typical time δt are expected at radius $r \sim \Gamma^2 c \delta t$, where Γ is the jet Lorentz factor. However, since the observed time is $t \sim r/\Gamma^2 c$, the dependence on the unknown Lorentz factor cancels, and the observed flaring time is similar in both low and high Lorentz factor GRBs. Similar argument holds for the ratio of flare widths to peak time.

6. Summary and Conclusion

In this paper, we considered the X-ray LCs of 89 GRBs. We find that 61 (69%) of all GRBs have flares, and 57 (64%) have plateaus. However, no correlation was found between the existence of flares and the existence of a plateau. We therefore conclude that the existence of flares is independent of the existence of an X-ray plateau.

We then analyzed the properties of flares that were detected in those 61 GRBs. Of those GRBs, 42 (68%) have a plateau, while 19 do not. We found no statistical difference between the flare peak times and the ratio of flare width to peak time, $w/t_{\text{pk}} \sim 1$ between GRBs with and without a plateau. From these results, presented in Section 3.1, we conclude that the flare properties of GRBs are similar regardless of the presence or absence of a plateau phase in GRBs X-ray LCs.

We then confronted these results with three leading theories discussed in the literature as a possible origin of the plateau: (i) late-time energy injection; (ii) observers located at different viewing angles; and (iii) emission during the coasting phase, which requires the terminal jet Lorentz factor to not exceed a few tens. We find that the former two models' predictions are inconsistent with the observed results. In a late energy injection model, one expects that at least some of the flares will occur at later times, and may be narrower than without it, which is not seen. Similarly, for an observer located off the jet axis, the observed flare time should appear later than for an observer located on the line of sight, due to different Doppler boosting. The predictions of the low Lorentz factor model, on the other hand, are consistent with the results presented here. For GRBs with low Lorentz factors, one expects the flares to originate at a smaller radius relative to GRBs with a larger Lorentz factor. But since the observed time depends on the Lorentz factor, an observer will see the flares at (average) similar times, regardless of the different Lorentz factors. Our results therefore provide independent support to the idea that the origin of the plateau phase is GRBs with a lower Lorentz factor, on the order of few tens, as presented in H. Dereli-Bégué et al. (2022).

This study, which employs an approach to fitting the underlying afterglow with physically motivated models and clearly defining the flare properties, can be expanded to a larger sample with X-ray data and extended using data obtained at different wavelengths, such as UV and optical, to address the debate between X-ray flares and optical flashes. Notably, the recent SVOM and upcoming ULTRASAT space telescopes aim to increase the number of GRBs detected in these bands by providing rapid, arcsecond-level localization of bursts to trigger ground-based facilities. In addition, combining data from Swift and SVOM could allow for a better sampling of the LC, in particular between the time range 10^3 and 10^4 s.

If correct, this model has a strong potential to provide valuable clues about the underlying physics of GRB progenitors and jet dynamics. Coasting Lorentz factors of

several tens that may be in a substantial fraction of GRBs could significantly release physical constraints on the jet acceleration, and progenitor properties. It is therefore of high importance to find independent measures that could validate or invalidate this idea. The results presented here suggest such a strong, independent support.

Acknowledgments

We wish to thank Dr. Paz Beniamini and Miss A. Gowri for enlightening discussions on the manuscript. We would also like to thank the anonymous referee for their thoughtful suggestions and comments. This work made use of data supplied by the UK Swift Science Data Centre at the University of Leicester. A.P., acknowledges support from the European Union via ERC consolidating grant #773062 (acronym O.M.J.) and from the Israel Space Agency via grant No. 6766. F.R. acknowledges support from the Swedish National Space Agency (2021-00180 and 2022-00205).

Facility: Swift.

Software: MultiNest.

Appendix A

Models Used for Fitting the Data

In our analysis, we consider the following models for fitting the underlying afterglow emission. First, we consider two classes of models, referring to the medium into which the blast wave expands: (i) the “wind” model, in which the ambient density drops with radius as $n(r) \propto r^{-2}$, and the “ISM” model, which assumes a constant ambient density profile, $n(r) \propto r^0$. These two different assumptions affect the evolution of the blast wave Lorentz factor, and are therefore considered separately. We further assume that electrons are accelerated to a power law in the propagating blast wave, with a power-law index p . The observed signal is due to synchrotron emission from these electrons. The spectral and temporal slopes depend on the observed frequency, relative to the characteristic synchrotron frequencies: the peak frequency, ν_m and the cooling frequency, ν_c . Different slopes are expected for $\{\nu_m, \nu_c\} < \nu^{\text{obs.}}$, $\nu_m < \nu^{\text{obs.}} < \nu_c$, etc. We refer to the nomenclature defined in H. Dereli-Bégué et al. (2022) to label the different models. Since we are focusing on data in the X-ray band obtained by the Swift-XRT instrument, our analysis considers the scenarios labeled as C/F and E in H. Dereli-Bégué et al. (2022), for which the time evolution of the spectrum is given by

$$\begin{aligned} \text{Case C/F: } & \{\nu_m, \nu_c\} < \nu^{\text{obs.}} \\ & \times F_\nu \propto \begin{cases} t_{\text{obs.}}^{(2-p)/2} \nu^{-p/2} & t_{\text{obs.}} < T_a, \\ t_{\text{obs.}}^{(2-3p)/4} \nu^{-p/2} & t_{\text{obs.}} > T_a, \end{cases} \end{aligned} \quad (\text{A1})$$

$$\begin{aligned} \text{Case E: } & \nu_m < \nu^{\text{obs.}} < \nu_c \\ & \times F_\nu \propto \begin{cases} t_{\text{obs.}}^{(1-p)/2} \nu^{-(p-1)/2} & t_{\text{obs.}} < T_a, \\ t_{\text{obs.}}^{(1-3p)/4} \nu^{-(p-1)/2} & t_{\text{obs.}} > T_a. \end{cases} \end{aligned} \quad (\text{A2})$$

Here, $t_{\text{obs.}}$ is the observed time and T_a is the end of the plateau time. According to our interpretation, this time marks the transition between the coasting and the decelerating phase of the expansion. In this transition, the index of the electron injection function p is assumed to be constant, thereby linking

the temporal slope before the plateau to that after the plateau, enforcing rigidity in our models.

For the ISM model, we refer to the two segments labeled as G and H in R. Sari et al. (1998):

$$\text{Case G: } \nu_m < \nu_{\text{obs.}} < \nu_c \\ \times F_\nu \propto t_{\text{obs.}}^{(3-3p)/4} \nu^{-(p-1)/2}, \quad (\text{A3})$$

$$\text{Case H: } \{\nu_m, \nu_c\} < \nu_{\text{obs.}} \\ \times F_\nu \propto t_{\text{obs.}}^{(2-3p)/4} \nu^{-p/2}. \quad (\text{A4})$$

In this case, we assume that the transition between the coasting phase and self-similar phase happens before the first Swift-XRT observations or during the steep decay. Consequently, in our analysis, we do not consider the coasting phase for the ISM models.

The cases C/F and E for the wind environment and cases G and H for the ISM environment represent different spectral regimes depending on the cooling state of the plasma behind the shock, namely on the position of the cooling frequency ν_c with respect to the injection frequency ν_m . Finally, on top of each emission model, we further consider the possibility of observing (i) a steep decay, assumed in this analysis to be associated with the end of the prompt phase, (ii) a jet break, and (iii) zero, one, or two flares. This led us to fit a total of 36 models to each observed afterglow LC. Twelve models are considered for the “wind” environment scenario, which differ by the existence/inexistence of a jet break, number of flares (zero, one, or two) and spectral regime (C/F or E). Twenty-four models are considered for the “ISM” case, which, in addition to the above, consider existence or inexistence of a steep decay (in the “wind” model, which is used to fit GRBs with a plateau, where a steep decay is always assumed to exist). The details of each model and their components are summarized in Table A1.

All afterglow components at the exception of the flares are assumed to be power-law functions of time, namely the flux in the X-ray band is $F_x(t) \propto t^a$. The power-law index a is motivated by the considered component and the physical scenario as described in the equations above, at the exception of the index of the fast decay, which is constrained to be greater than 2. All components making an empirical afterglow model form a continuous function in time. The analysis is performed in log space, meaning that the variable becomes $T \equiv \log(t)$ and the observable is $\mathcal{F} \equiv \log(F)$. For instance, a model of an afterglow in a wind environment with a steep decay, a jet break, and such that $\{\nu_m, \nu_c\} \ll \nu_{\text{obs.}}$, is expressed as

$$\mathcal{F} = \begin{cases} \alpha T + A & T < T_1, \\ \beta T + A + (\alpha - \beta)T_1 & T_1 < T < T_2, \\ \zeta T + A + (\alpha - \beta)T_1 + (\beta - \zeta)T_2 & T_2 < T < T_3, \\ (\zeta + q)T + A + (\alpha - \beta)T_1 + (\beta - \zeta)T_2 + (\zeta - \eta)T_3 & T_3 > T. \end{cases} \quad (\text{A5})$$

Here, A represents the normalization of the flux, T_1 is the transition time between the steep decay and the first afterglow segment, namely the plateau, $T_2 \equiv T_a$ is the time at which the blast wave transitions from the plateau to a steeper decay (interpreted as coasting to the decelerating phase), and T_3 is the time of the jet break. For this specific regime, the parameters β and ζ are not independent: they both depend on the power-law index p of the injected electrons at the shock front. We use this constraint, by setting β and ζ to the parameter dependencies presented in Equations (A1), (A2), (A3), and (A4), and

Table A1
Comparison of Models for Different Theoretical Scenarios

Environment	Model Name	Steep Decay	Jet Break	Number of Flares
Wind	Case C/F and Case E			
	C1/E1	Yes	No	0
	C2/E2	Yes	Yes	0
	C3/E3	Yes	No	1
	C4/E4	Yes	No	2
	C5/E5	Yes	Yes	1
	C6/E6	Yes	Yes	2
ISM	Case H and Case G			
	H1/G1	No	No	0
	H2/G2	No	No	1
	H3/G3	No	No	2
	H4/G4	Yes	No	0
	H5/G5	Yes	No	1
	H6/G6	Yes	No	2
	H7/G7	No	Yes	0
	H8/G8	No	Yes	1
	H9/G9	No	Yes	2
	H10/G10	Yes	Yes	0
	H11/G11	Yes	Yes	1
	H12/G12	Yes	Yes	2

Note. For wind scenarios (cases C/F and E), the models include conditions for a steep decay, a jet break, and a number of flares. All models incorporate the early steep decay phase, with an optional jet break and flare presence. For ISM scenarios (cases H and G), the models include similar conditions with additional differentiation, where the early steep decay is also optional. The table details the presence of a steep decay, jet break, and the number of flares for each model.

consider p to be the free model parameter. For the example of Equation (A5), we have $\beta = (2 - p)/2$ and $\zeta = (2 - 3p)/4$. In addition, after the jet break, the afterglow slope is steeper than ζ and rather than fitting directly for the slope, we fit for the difference q between the post-jet-break slope and ζ , such that the new slope is $\zeta + q$. We allow for the extra degree of freedom in the choice of the value of q , as the jet break is not sharp, but rather is observed over a long duration, in particular for observers that are off the jet axis. These techniques add some rigidity to the models and allow for a straightforward interpretation of the results. An example of the fitting results is presented in Figure A1 in Appendix A.1.

A.1. Example Fit to the X-Ray Light Curve of GRB 190719C

To visualize the fitting process, in Figure A1 (left top), we illustrate the X-ray count LC of GRB 190719C obtained by the Swift-XRT instrument. The data are fitted in log scale, therefore, for consistency we present the data in log scale as well. The data are superposed with the fit results (blue) from a selected best model where the three segment broken power-law model, i.e., with two break times, and two Norris functions are used to fit two flares. It represents the case C/F in the wind where a steep decay, plateau phase, and a late afterglow decay are present, but no jet break. This model is shown as C4 in Table A1. In Figure A1 (left bottom), we present the residuals between the best model and the data, which shows how well the model

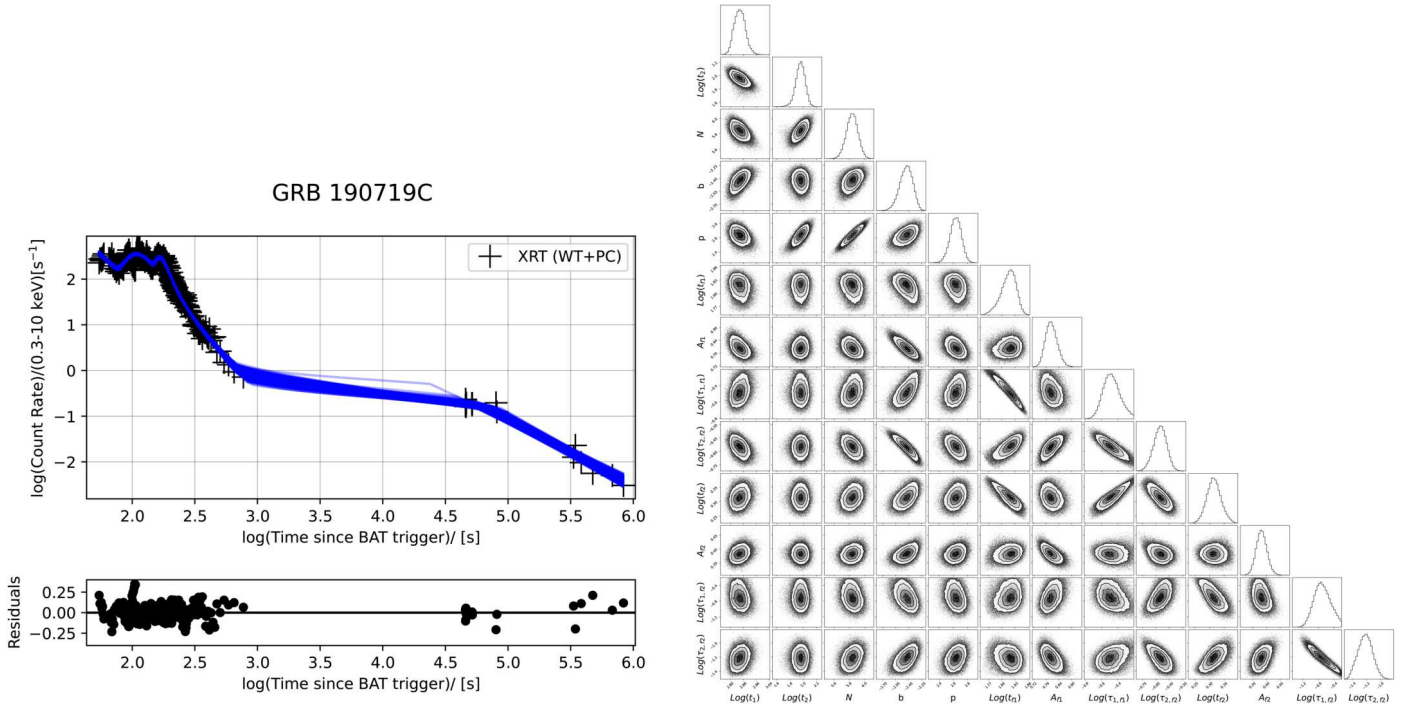


Figure A1. Left top: the X-ray LC of GRB 190719C. The black crosses represent the XRT-WTSLEW, XRT-WT, and XRT-PC mode data. The errors correspond to a significance of 1σ . The blue lines represent the posterior distributions of the best-fit model. Left bottom: the residuals between the best model and the data. Right: corner plot of the posterior probability distributions of the fit parameters and the covariances between the fit parameters.

describes the data. The corner plot of the posterior probability distributions of the fit parameters and the covariances between the fit parameters is displayed in Figure A1 (right).

Appendix B

Bursts Excluded from the Sample

Out of the 100 GRBs in our sample, we exclude 11 GRBs listed in Table B1. The exclusion criteria were the misidentification of flares, which compromised the underlying afterglow emission and failures of the different afterglow models to adequately fit the data. When this happened, the identified flares extend more than the data, most of the time up to $>10^5$ s, which corresponds to the more than half of the dynamical range. As a result, the allowed variability in the flare shape replaces the underlying afterglow, which is at nearly all times dominated by flare emission. Therefore, such a exclusion was done to avoid misinterpretation of the model parameters.

Table B1
The List of Excluded 11 Gamma-Ray Bursts from the Main Sample

GRB Name	w (s)	$E_{\text{iso},f}$ (erg)
221009A	0.4×10^5	10^{51}
210610A	0.7×10^7	10^{52}
210104A	0.5×10^7	10^{51}
201221A	0.3×10^5	10^{52}
190114C	0.3×10^7	10^{51}
170728B	0.3×10^7	10^{52}
161129A	0.8×10^7	10^{51}
160117B	0.4×10^8	10^{51}
150910A	0.2×10^7	10^{52}
150403A	0.1×10^8	10^{53}
140614A	0.8×10^8	10^{52}

Note. Column (1): GRB name. Column (2): the flare width. Column (3): the flare's isotropic energy.

Appendix C

Sample of 61 Gamma-Ray Bursts with Flares and Derived Parameters

In our analysis, the fit parameters are computed using the maximum posterior estimate method. The derived parameters and their errors are calculated using the marginalized posterior distributions. As discussed in Section 2.4, the selection of the best-fit models is based on the AIC and AICc criteria. The

results show that the AICc condition is consistently satisfied by the data. Additionally, in most cases, the AIC condition is also met by the same model. Therefore, we only present the AICc in Table C1, along with the derived parameters obtained from the best-fit parameters, as well as GRB name, redshift z and the name of the best models. The parameter errors are computed by using the credible intervals (e.g., 68% for 1σ) derived directly from the posterior samples of the fit parameters.

Table C1
Derived Parameters for Selected Gamma-Ray Bursts with Flares (Part 1)





GRB Name	z	Best Model	AICc	t_{pk} (s)	w (s)	k	$E_{\text{iso},f}$ (10^{50} erg)	w/t_{pk}	$\Delta F_{\text{flare}}/F_{\text{cont.}}$
220117A	4.96	C4	251	$189^{+1.6}_{-2.04}$ 1124^{+67}_{-68}	434^{+240}_{-157} 5203^{+1054}_{-1499}	$0.37^{+0.03}_{-0.03}$ $0.45^{+0.01}_{-0.01}$	$360^{+22.6}_{-25.5}$ $373^{+55.1}_{-68.2}$	$2.3^{+1.3}_{-0.8}$ $4.6^{+0.8}_{-1.2}$	$9.7^{+4.2}_{-2.6}$ $6.9^{+2.5}_{-1.9}$
220101A	4.62	C5	801	$167^{+6.7}_{-7.8}$	298^{+68}_{-75}	$0.50^{+0.02}_{-0.02}$	5769^{+785}_{-115}	$1.8^{+0.3}_{-0.4}$	$11.2^{+4.4}_{-3.6}$
211024B	1.11	C4	442	6621^{+169}_{-186} $1.4 \times 10^{+145}_{-153}$	$1.4 \times 10^{+2 \times 10^4}_{-0.6 \times 10^4}$ $1.1 \times 10^{+5+1.6 \times 10^4}_{-2.6 \times 10^4}$	$0.38^{+0.05}_{-0.05}$ $0.32^{+0.01}_{-0.01}$	$123^{+15.4}_{-31.1}$ $103^{+3.5}_{-3.5}$	$2.1^{+3.0}_{-1.0}$ $7.9^{+1.2}_{-1.9}$	178^{+52}_{-77} $36.5^{+13.5}_{-10.5}$
210905A	6.32	G3	272	$98^{+1.1}_{-1.2}$ $371^{+1.4}_{-1.2}$	155^{+91}_{-69} $140^{+79}_{-16.1}$	$0.37^{+0.04}_{-0.03}$ $0.75^{+0.01}_{-0.02}$	$239^{+18.6}_{-21.5}$ 1208^{+101}_{-91}	$1.6^{+0.9}_{-0.7}$ $0.4^{+0.05}_{-0.04}$	$2.3^{+0.3}_{-0.2}$ $17.4^{+1.0}_{-0.9}$
210722A	1.15	G9	278	$124^{+0.8}_{-0.8}$ 8545^{+439}_{-468}	1210^{+54}_{-102} $3.8 \times 10^{+1 \times 10^4}_{-1.2 \times 10^4}$	$0.30^{+0.004}_{-0.004}$ $0.45^{+0.02}_{-0.01}$	$11.9^{+0.5}_{-0.5}$ $11.7^{+1.1}_{-1.2}$	$9.7^{+0.4}_{-0.8}$ $4.4^{+1.0}_{-1.3}$	$2.3^{+0.1}_{-0.1}$ $3.3^{+0.5}_{-0.4}$
210702A	1.16	H8	523	5245^{+308}_{-435}	$1 \times 10^{+4+1.3 \times 10^4}_{-0.6 \times 10^4}$	$0.47^{+0.09}_{-0.05}$	$37.9^{+13.3}_{-10.9}$	$2.0^{+2.4}_{-1.1}$	$1.0^{+0.2}_{-0.2}$
210610B	1.13	C5	651	$102^{+1.7}_{-1.9}$	$80^{+2.7}_{-2.4}$	$0.57^{+0.02}_{-0.02}$	$46.9^{+4.3}_{-0.9}$	$0.8^{+0.03}_{-0.03}$	$37.6^{+5.3}_{-3.9}$
210504A	2.08	E3	104	$460^{+6.9}_{-7.0}$	210^{+601}_{-134}	$0.41^{+0.12}_{-0.10}$	$11.8^{+1.9}_{-2.9}$	$0.5^{+1.3}_{-0.3}$	$4.6^{+0.8}_{-0.7}$
210420B	1.40	E3	121	$716^{+42.9}_{-33.6}$	438^{+362}_{-180}	$0.64^{+0.09}_{-0.12}$	$5.1^{+1.6}_{-1.4}$	$0.6^{+0.5}_{-0.3}$	$2.8^{+0.4}_{-0.3}$
210411C	2.83	G9	70	$174^{+3.9}_{-4.7}$ 663^{+113}_{-92}	$101^{+308}_{-37.7}$ 1573^{+1650}_{-865}	$0.48^{+0.12}_{-0.12}$ $0.47^{+0.06}_{-0.04}$	$32.9^{+2.1}_{-8.1}$ $30.5^{+11.6}_{-10.8}$	$0.6^{+0.2}_{-0.2}$ $2.4^{+2.1}_{-1.2}$	$4.9^{+0.7}_{-0.6}$ $0.9^{+0.2}_{-0.2}$
201104B	1.95	C3	112	$202^{+3.2}_{-3.6}$ $455^{+1.9}_{-1.7}$	303^{+913}_{-242} 1774^{+348}_{-221}	$0.30^{+0.12}_{-0.06}$ $0.31^{+0.01}_{-0.01}$	$3.1^{+0.65}_{-0.68}$ $168^{+2.3}_{-2.2}$	$1.5^{+4.5}_{-0.5}$ $3.9^{+0.8}_{-0.5}$	$0.7^{+0.1}_{-0.1}$ $17.8^{+1.0}_{-0.9}$
200205B	1.47	C6	523	$534^{+2.9}_{-2.9}$ $169^{+1.9}_{-2.0}$	$183^{+27.5}_{-25.8}$ 1382^{+140}_{-244}	$0.74^{+0.01}_{-0.01}$ $0.33^{+0.01}_{-0.004}$	$47.5^{+2.1}_{-2.4}$ $28.9^{+1.0}_{-0.9}$	$0.3^{+0.05}_{-0.05}$ $8.2^{+0.8}_{-1.4}$	$2.3^{+0.2}_{-0.2}$ $2.5^{+0.1}_{-0.1}$
191221B	1.15	C5	954	$1524^{+29.4}_{-26.6}$ $175^{+1.1}_{-1.1}$	1460^{+280}_{-154} 202^{+286}_{-96}	$0.54^{+0.03}_{-0.03}$ $0.35^{+0.06}_{-0.06}$	$28.9^{+1.0}_{-0.9}$ 589^{+20}_{-25}	$1.0^{+0.2}_{-1.6}$ $1.2^{+0.5}_{-0.5}$	$3.0^{+0.1}_{-0.1}$ $1.4^{+0.1}_{-0.1}$
190829A	0.08	C5	789	$133^{+3.2}_{-3.0}$ $232^{+6.5}_{-10.1}$	266^{+167}_{-80} $39.8^{+37.2}_{-9.1}$	$0.43^{+0.03}_{-0.04}$ $0.55^{+0.09}_{-0.11}$	$154^{+9.4}_{-9.5}$ 67^{+26}_{-22}	$2.0^{+1.3}_{-0.6}$ $0.2^{+0.2}_{-0.04}$	$5.4^{+0.4}_{-0.4}$ $3.0^{+1.6}_{-0.9}$
190719C	2.47	C4	685	1688^{+700}_{-219} $100^{+0.5}_{-0.5}$	4800^{+6242}_{-4158} 790^{+350}_{-368}	$0.45^{+0.10}_{-0.06}$ $0.22^{+0.02}_{-0.02}$	$34.2^{+2.4}_{-2.5}$ $36.6^{+2.5}_{-2.5}$	$2.5^{+0.8}_{-2.1}$ $7.9^{+3.5}_{-3.7}$	$0.9^{+0.8}_{-0.2}$ $1.3^{+0.1}_{-0.1}$
190106A	1.86	C6	290	$258^{+38.9}_{-12.1}$ $168^{+1.2}_{-1.2}$	141^{+289}_{-96} 1434^{+121}_{-183}	$0.56^{+0.15}_{-0.15}$ $0.32^{+0.01}_{-0.004}$	$1.5^{+1.7}_{-0.61}$ $798^{+16.4}_{-16.7}$	$0.5^{+0.9}_{-0.3}$ $8.5^{+0.7}_{-1.1}$	$0.7^{+0.2}_{-0.1}$ $7.2^{+0.9}_{-0.8}$
181110A	1.51	C6	588	$118^{+2.1}_{-2.1}$ $242^{+0.6}_{-0.6}$	$984^{+36.1}_{-67}$ 2331^{+64}_{-123}	$0.34^{+0.01}_{-0.004}$ $0.31^{+0.002}_{-0.004}$	$536^{+17.9}_{-18.3}$ $942^{+10.3}_{-0.3}$	$8.3^{+0.3}_{-0.6}$ $9.6^{+0.5}_{-0.5}$	$6.9^{+0.6}_{-0.5}$ $6.2^{+0.1}_{-0.1}$
181020A	2.94	G12	1669	$375^{+0.7}_{-0.8}$ $140^{+13.2}_{-27.0}$	2623^{+1565}_{-1311} 94^{+242}_{-50}	$0.21^{+0.02}_{-0.01}$ $0.53^{+0.18}_{-0.18}$	$103^{+4.7}_{-4.5}$ $1.3^{+1.0}_{-0.6}$	$7.0^{+4.2}_{-3.5}$ $0.8^{+1.5}_{-0.4}$	$1.1^{+0.04}_{-0.04}$ $1.1^{+0.7}_{-0.7}$
181010A	1.39	C5	208	$2411^{+38.1}_{-37.3}$ 5226^{+2268}_{-1252}	2927^{+2965}_{-1228} 2784^{+18002}_{-1935}	$0.43^{+0.06}_{-0.05}$ $0.44^{+0.18}_{-0.12}$	$0.26^{+0.06}_{-0.07}$ $0.3^{+1.7}_{-0.2}$	$1.2^{+1.2}_{-0.5}$ $0.5^{+3.0}_{-0.3}$	$1.4^{+0.1}_{-0.1}$ $1.9^{+18.4}_{-1.2}$
180728A	0.12	E4	978	$110^{+1.8}_{-1.7}$ $362^{+5.8}_{-5.4}$	$69^{+17.4}_{-12.5}$ 2675^{+177}_{-315}	$0.71^{+0.04}_{-0.04}$ $0.36^{+0.01}_{-0.004}$	$32.2^{+3.4}_{-3.2}$ $53.7^{+2.5}_{-2.5}$	$0.6^{+0.2}_{-0.1}$ $7.4^{+0.5}_{-0.8}$	$1.2^{+0.1}_{-0.1}$ $1.4^{+0.1}_{-0.1}$
180720B	0.65	C4	3434	$192^{+1.0}_{-0.7}$ $444^{+5.6}_{-7.0}$	$87^{+10.6}_{-6.7}$ 403^{+60}_{-65}	$0.66^{+0.02}_{-0.02}$ $0.63^{+0.01}_{-0.02}$	$309^{+12.1}_{-9.1}$ $524^{+16.5}_{-22.2}$	$0.5^{+0.1}_{-0.04}$ $0.9^{+0.1}_{-0.1}$	$26.9^{+1.9}_{-1.3}$ $53^{+4.2}_{-5.3}$
180624A	2.86	E4	1487	$165^{+5.4}_{-5.9}$ 5956^{+807}_{-841}	918^{+206}_{-280} $1.1 \times 10^{+4+1.4 \times 10^4}_{-0.5 \times 10^4}$	$0.40^{+0.02}_{-0.01}$ $0.49^{+0.09}_{-0.04}$	$61.9^{+2.9}_{-3.1}$ $8.2^{+4.1}_{-2.8}$	$5.6^{+1.2}_{-0.5}$ $1.9^{+2.3}_{-0.8}$	$3.9^{+0.6}_{-0.5}$ $1.1^{+0.2}_{-0.2}$
180620B	1.12	E6	367	$166^{+1.1}_{-1.1}$ $234^{+2.3}_{-2.0}$	$150^{+38.8}_{-25.8}$ $202^{+58}_{-41.2}$	$0.43^{+0.02}_{-0.02}$ $0.39^{+0.02}_{-0.03}$	$161^{+4.5}_{-7.1}$ $44^{+4.5}_{-3.7}$	$0.9^{+0.2}_{-0.2}$ $0.9^{+0.2}_{-0.2}$	$94^{+6.2}_{-6.9}$ $2.3^{+0.5}_{-0.3}$
180325A	2.25	C3	381	$81^{+0.8}_{-0.9}$ $181^{+1.8}_{-1.8}$	$15.1^{+3.0}_{-0.9}$ $86^{+161}_{-43.7}$	$0.56^{+0.06}_{-0.06}$ $0.42^{+0.07}_{-0.08}$	$93.8^{+9.5}_{-8.1}$ $4.8^{+0.7}_{-10.6}$	$0.2^{+0.03}_{-0.01}$ $0.5^{+0.9}_{-0.2}$	$14.0^{+1.2}_{-1.0}$ $4.5^{+1.0}_{-0.7}$
180205A	1.41	G8	89	$337^{+19.0}_{-17.1}$ 5285^{+211}_{-258}	558^{+131}_{-94} $2.8 \times 10^{+1 \times 10^4}_{-1.1 \times 10^4}$	$0.51^{+0.02}_{-0.03}$ $0.38^{+0.02}_{-0.01}$	$225^{+20.3}_{-20.0}$ $120^{+9.2}_{-9.2}$	$1.6^{+0.3}_{-0.2}$ $5.3^{+1.7}_{-2.1}$	$4.5^{+0.8}_{-0.8}$ $4.8^{+0.2}_{-0.2}$
171222A	2.41	C3	212	$170714A$	$1.3 \times 10^{+4+82}_{-86}$ $1.2 \times 10^{+5+0.8 \times 10^4}_{-1.5 \times 10^4}$	$0.32^{+0.01}_{-0.004}$	$81.8^{+2.2}_{-2.2}$	$8.8^{+0.6}_{-1.1}$	$7.6^{+0.6}_{-0.5}$
170705A	2.01	C5	992	$217^{+0.7}_{-0.7}$ $152^{+8.6}_{-7.3}$	$1800^{+19.0}_{-39.4}$ $162^{+24.2}_{-12.7}$	$0.35^{+0.001}_{-0.001}$ $0.58^{+0.03}_{-0.03}$	$245^{+2.1}_{-2.1}$ $3.6^{+0.2}_{-0.2}$	$8.3^{+0.1}_{-0.2}$ $1.1^{+0.1}_{-0.1}$	$76^{+2.9}_{-2.9}$ $1.8^{+0.2}_{-0.1}$
170607A	0.56	E4	576	9050^{+685}_{-708}	$3.5 \times 10^{+4+1.5 \times 10^4}_{-1.5 \times 10^4}$	$0.45^{+0.03}_{-0.02}$	$1.9^{+0.4}_{-0.5}$	$3.8^{+1.5}_{-1.5}$	$0.9^{+0.1}_{-0.1}$
170604A	1.33	3H	535	$130^{+2.4}_{-2.2}$ $364^{+1.0}_{-1.1}$	$42.0^{+2.8}_{-3.0}$ 2623^{+1037}_{-1192}	$0.73^{+0.01}_{-0.01}$ $0.28^{+0.02}_{-0.01}$	$37.3^{+3.3}_{-3.1}$ $84^{+1.9}_{-1.8}$	$0.3^{+0.02}_{-0.02}$ $7.2^{+2.8}_{-3.3}$	$9.5^{+0.9}_{-0.8}$ $12.1^{+0.4}_{-0.4}$

Table C1
(Continued)

GRB Name	z	Best Model	AICc	t_{pk} (s)	w (s)	k	$E_{\text{iso},f}$ (10^{50} erg)	w/t_{pk}	$\Delta F_{\text{flare}}/F_{\text{cont.}}$
170531B	2.37	G3	397	$168^{+0.4}_{-0.4}$ $576^{+0.6}_{-0.6}$	$255^{+40.1}_{-39.7}$ 711^{+294}_{-187}	$0.38^{+0.01}_{-0.01}$ $0.33^{+0.02}_{-0.02}$	$52^{+1.7}_{-2.3}$ $98^{+5.2}_{-4.3}$	$126^{+1.3}_{-1.4}$ $76^{+1.1}_{-1.1}$	$48.2^{+1.8}_{-2.5}$ $62^{+2.0}_{-2.8}$
170519A	0.82	E4	820	$203^{+0.4}_{-0.4}$ 2153^{+1824}_{-883}	$67^{+2.9}_{-2.8}$ 2099^{+2432}_{-1028}	$0.72^{+0.01}_{-0.01}$ $0.64^{+0.12}_{-0.12}$	$28.4^{+0.5}_{-0.5}$ $2.1^{+2.0}_{-1.0}$	$0.3^{+0.01}_{-0.01}$ $0.9^{+0.5}_{-0.5}$	$49.7^{+1.7}_{-1.7}$ $2.6^{+5.5}_{-1.2}$
170405A	3.51	H9	420	$162^{+0.7}_{-0.7}$ 6555^{+1139}_{-1245}	$131^{+95}_{-44.8}$ $1.6 \times 10^{4+1.7 \times 10^4}_{-1.0 \times 10^3}$	$0.36^{+0.03}_{-0.04}$ $0.48^{+0.08}_{-0.03}$	$242^{+0.3}_{-11.7}$ $242^{+10.3}_{-11.7}$	$0.8^{+0.6}_{-0.3}$ $2.5^{+2.2}_{-1.4}$	$2.7^{+0.1}_{-0.1}$ $2.0^{+0.8}_{-0.4}$
170202A	3.65	C3	108	$100^{+4.1}_{-3.2}$	$41.0^{+41.1}_{-15.1}$	$0.65^{+0.09}_{-0.15}$	$18.5^{+6.3}_{-4.5}$	$0.4^{+0.4}_{-0.1}$	$0.6^{+0.1}_{-0.04}$
170113A	1.99	C4	273	$93^{+0.4}_{-0.4}$ $94^{+0.8}_{-0.9}$	$21.1^{+14.3}_{-8.3}$ 581^{+163}_{-143}	$0.44^{+0.06}_{-0.05}$ $0.34^{+0.01}_{-0.01}$	$78.4^{+1.6}_{-1.5}$ $25.8^{+4.6}_{-5.8}$	$0.2^{+0.2}_{-0.1}$ $6.2^{+1.7}_{-1.5}$	$1.8^{+0.3}_{-0.2}$ $10.3^{+1.4}_{-1.3}$
161219B	0.15	C6	737	2480^{+82}_{-79} $406^{+4.2}_{-4.3}$	$14, 036^{+1626}_{-2806}$ $315^{+55}_{-45.4}$	$0.42^{+0.01}_{-0.01}$ $0.67^{+0.03}_{-0.03}$	$0.11^{+0.01}_{-0.01}$ $0.4^{+0.03}_{-0.03}$	$5.7^{+0.6}_{-0.6}$ $0.8^{+0.1}_{-0.1}$	$4.8^{+0.7}_{-0.6}$ $38.6^{+2.9}_{-2.6}$
161117A	1.55	G12	560	$124^{+0.6}_{-0.6}$ 7844^{+480}_{-512}	$168^{+30.2}_{-23.9}$ $2.7 \times 10^{4+1.3 \times 10^4}_{-1.2 \times 10^4}$	$0.45^{+0.01}_{-0.01}$ $0.46^{+0.03}_{-0.02}$	$364^{+7.9}_{-8.9}$ $27.8^{+4.4}_{-4.5}$	$1.4^{+0.2}_{-0.2}$ $1.8^{+0.2}_{-0.2}$	$42.4^{+1.6}_{-1.5}$ $1.8^{+0.2}_{-0.2}$
161108A	1.16	G6	416	$148^{+2.8}_{-2.8}$ 1398^{+1175}_{-557}	307^{+82}_{-72} 420^{+3034}_{-315}	$0.46^{+0.02}_{-0.02}$ $0.37^{+0.13}_{-0.11}$	$37.5^{+2.1}_{-3.3}$ $3.6^{+23.6}_{-3.2}$	$2.1^{+0.5}_{-0.5}$ $0.3^{+1.9}_{-0.2}$	$3.6^{+0.3}_{-0.3}$ $32.3^{+29.4}_{-29.3}$
161017A	2.01	C6	1562	$409^{+1.2}_{-1.2}$ $201^{+1.4}_{-1.4}$	4630^{+295}_{-357} $1712^{+35.1}_{-64}$	$0.24^{+0.004}_{-0.003}$ $0.34^{+0.003}_{-0.003}$	$337^{+6.8}_{-6.7}$ $88^{+2.8}_{-2.8}$	$11.3^{+0.7}_{-1.4}$ $8.5^{+0.2}_{-0.3}$	$1.7^{+0.1}_{-0.1}$ $3.2^{+0.1}_{-0.1}$
160804A	0.74	G12	1464	$433^{+2.2}_{-2.2}$ $1.5 \times 10^{4+2 \times 10^3}_{-2 \times 10^3}$	4194^{+87}_{-153} $2.3 \times 10^{4+3.8 \times 10^4}_{-1.0 \times 10^4}$	$0.31^{+0.004}_{-0.003}$ $0.49^{+0.11}_{-0.06}$	$11^{+0.4}_{-0.4}$ $0.7^{+0.2}_{-0.2}$	$1.5^{+0.1}_{-0.1}$ $1.5^{+2.3}_{-0.6}$	$1.5^{+0.1}_{-0.1}$ $0.7^{+0.2}_{-0.2}$
160425A	0.56	G5	1004	$300^{+0.6}_{-0.6}$	$287^{+75}_{-30.9}$	$0.40^{+0.01}_{-0.01}$	$34.1^{+0.4}_{-0.4}$	$1.0^{+0.1}_{-0.1}$	$115^{+5.3}_{-6.4}$
160410AS	1.72	E3	77	$192^{+32.4}_{-39.3}$	600^{+479}_{-416}	$0.45^{+0.07}_{-0.04}$	$7.1^{+3.0}_{-2.3}$	$3.0^{+2.1}_{-1.9}$	$1.1^{+1.4}_{-0.4}$
160228A	1.64	H8	95	$181^{+2.8}_{-3.3}$	75^{+568}_{-61}	$0.39^{+0.13}_{-0.13}$	$0.6^{+2.5}_{-2.1}$	$0.4^{+1.5}_{-0.3}$	$1.0^{+0.5}_{-0.3}$
160227A	2.38	E4	859	$215^{+0.8}_{-0.8}$ $422^{+1.1}_{-1.0}$	$83^{+6.7}_{-6.3}$ $345^{+16.8}_{-16.0}$	$0.68^{+0.01}_{-0.01}$ $0.80^{+0.003}_{-0.004}$	$186^{+4.9}_{-5.2}$ $137^{+3.1}_{-3.0}$	$0.4^{+0.03}_{-0.03}$ $0.8^{+0.03}_{-0.03}$	$16.4^{+0.7}_{-0.7}$ $9.9^{+0.7}_{-0.6}$
160131A	0.97	E4	582	$197^{+8.0}_{-11.3}$ 6948^{+296}_{-297}	871^{+204}_{-268} $29, 744^{+17935}_{-15924}$	$0.46^{+0.02}_{-0.01}$ $0.39^{+0.05}_{-0.03}$	$4.4^{+3.2}_{-1.2}$ $6.2^{+1.0}_{-1.1}$	$1.9^{+0.6}_{-0.5}$ $4.3^{+2.5}_{-2.2}$	$1.9^{+0.6}_{-0.5}$ $0.6^{+0.1}_{-0.04}$
151027B	4.06	C3	66	3626^{+944}_{-708}	3263^{+14307}_{-2535}	$0.47^{+0.23}_{-0.13}$	35.7^{+121}_{-131}	$1.2^{+3.1}_{-0.9}$	$2.3^{+40.7}_{-0.9}$
151027A	0.81	C6	909	$132^{+0.4}_{-0.4}$ $307^{+1.9}_{-1.8}$	1180^{+121}_{-196} 3038^{+205}_{-380}	$0.30^{+0.01}_{-0.003}$ $0.28^{+0.01}_{-0.004}$	$49^{+0.82}_{-0.81}$ $4.9^{+0.2}_{-0.2}$	$9.0^{+0.9}_{-1.5}$ $9.9^{+0.7}_{-1.2}$	$35.8^{+1.9}_{-1.9}$ $1.7^{+0.1}_{-0.1}$
151021A	2.33	C4	294	$232^{+22.8}_{-11.8}$ $129^{+1.0}_{-1.2}$	185^{+323}_{-77} 1046^{+167}_{-242}	$0.46^{+0.09}_{-0.10}$ $0.31^{+0.01}_{-0.01}$	$352^{+1.2}_{-1.2}$ $20.5^{+6.5}_{-5.1}$	$0.8^{+1.4}_{-0.3}$ $8.1^{+1.3}_{-1.9}$	$1.1^{+0.2}_{-0.1}$ $4.3^{+0.3}_{-0.4}$
150821A	0.76	G6	670	$714^{+8.4}_{-7.6}$ $1126^{+5.5}_{-5.6}$	633^{+154}_{-87} 264^{+341}_{-148}	$0.50^{+0.02}_{-0.03}$ $0.36^{+0.08}_{-0.07}$	$7.0^{+0.73}_{-0.67}$ $0.53^{+0.1}_{-0.1}$	$0.9^{+0.2}_{-0.1}$ $0.2^{+0.3}_{-0.1}$	$1.7^{+0.05}_{-0.04}$ $0.7^{+0.1}_{-0.1}$
150818A	0.28	E3	301	$79^{+0.3}_{-0.3}$	421^{+435}_{-291}	$0.19^{+0.04}_{-0.02}$	$1.03^{+0.1}_{-0.1}$	$5.3^{+5.5}_{-3.7}$	$3.1^{+0.3}_{-0.3}$
150727A	0.31	E3	473	825^{+52}_{-62}	4008^{+704}_{-1111}	$0.45^{+0.01}_{-0.01}$	$0.2^{+0.02}_{-0.02}$	$4.9^{+0.7}_{-1.2}$	$1.2^{+0.1}_{-0.1}$
150314A	1.76	G11	704	$1.1 \times 10^{4+4.3 \times 10^3}_{-1.5 \times 10^3}$	$6.4 \times 10^{4+4 \times 10^6}_{-3.5 \times 10^4}$	$0.77^{+0.08}_{-0.06}$	$98^{+25.1}_{-16.2}$	$5.8^{+257}_{-3.0}$	$1.5^{+0.2}_{-0.2}$
150206A	2.09	H3	813	1911^{+92}_{-167} $2362^{+4.5}_{-4.4}$	$11, 386^{+5574}_{-5633}$ $2.0 \times 10^{4+8.6 \times 10^3}_{-8.8 \times 10^3}$	$0.32^{+0.03}_{-0.02}$ $0.21^{+0.02}_{-0.01}$	1722^{+539}_{-199} $431^{+35.6}_{-31.8}$	$6.1^{+2.7}_{-2.9}$ $8.3^{+3.6}_{-3.7}$	$8.1^{+2.5}_{-0.7}$ $1.6^{+0.2}_{-0.2}$
141221A	1.45	H3	69	$358^{+33.7}_{-28.4}$ $345^{+8.0}_{-7.8}$	590^{+748}_{-231} 431^{+1394}_{-356}	$0.50^{+0.06}_{-0.05}$ $0.33^{+0.16}_{-0.08}$	$14.1^{+3.4}_{-2.3}$ $4.1^{+1.5}_{-1.5}$	$1.6^{+1.9}_{-0.5}$ $1.1^{+3.9}_{-0.9}$	$4.4^{+1.1}_{-0.9}$ $1.6^{+0.4}_{-0.4}$
141121A	1.47	C4	882	$606^{+31.1}_{-25.2}$ 6671^{+207}_{-267}	244^{+338}_{-146} $2.6 \times 10^{4+1.6 \times 10^4}_{-1.4 \times 10^4}$	$0.70^{+0.07}_{-0.13}$ $0.40^{+0.05}_{-0.02}$	$23.7^{+9.2}_{-10.7}$ $42.2^{+3.6}_{-6.4}$	$0.4^{+0.5}_{-0.2}$ $3.9^{+2.1}_{-2.5}$	$2.8^{+0.6}_{-0.4}$ $13.8^{+3.8}_{-2.5}$
140907A	1.21	C3	111	$206^{+26.5}_{-18.7}$	601^{+766}_{-437}	$0.38^{+0.08}_{-0.05}$	$2.6^{+1.1}_{-1.0}$	$2.8^{+3.4}_{-2.0}$	$3.9^{+2.1}_{-1.2}$
140710A	0.56	G2	47	$365^{+12.4}_{-15.3}$	$140^{+131}_{-35.1}$	$0.60^{+0.12}_{-0.16}$	$0.3^{+0.7}_{-0.5}$	$0.4^{+0.3}_{-0.1}$	$10.4^{+2.3}_{-1.9}$
140703A	3.14	C5	176	$120^{+1.6}_{-1.7}$	$13.0^{+21.5}_{-3.0}$	$0.52^{+0.08}_{-0.14}$	58^{+24}_{-14}	$0.1^{+0.2}_{-0.1}$	$0.8^{+0.1}_{-0.1}$
140629A	2.28	C5	119	$202^{+38.7}_{-51}$	229^{+380}_{-102}	$0.52^{+0.09}_{-0.07}$	$8.5^{+9.0}_{-3.1}$	$1.1^{+0.3}_{-0.3}$	$1.5^{+0.9}_{-0.4}$

Note. Column (1): GRB name. Column (2): redshift. Column (3): best model. Column (4): AICc of the best model. Columns (5)–(10): derived parameters with their errors: flare peak time, flare width, flare asymmetry, total flare isotropic energy in units of 10^{50} erg, flare width to the flare peak time ratio, and flare peak flux-to-underlying continuum ratio. When the best model has two flares, the entry corresponding to this GRB is on two rows.

ORCID iDs

H. Dereli-Bégué  <https://orcid.org/0000-0002-8852-7530>
A. Pe’er  <https://orcid.org/0000-0001-8667-0889>
D. Bégué  <https://orcid.org/0000-0003-4477-1846>
F. Ryde  <https://orcid.org/0000-0002-9769-8016>

References

Abdo, A. A., Ackermann, M., Ajello, M., et al. 2011, *ApJL*, **734**, L27
Barthelmy, S. D., Cannizzo, J. K., Gehrels, N., et al. 2005, *ApJL*, **635**, L133

Beniamini, P., Duque, R., Daigne, F., & Mochkovitch, R. 2020a, *MNRAS*, **492**, 2847
Beniamini, P., Granot, J., & Gill, R. 2020b, *MNRAS*, **493**, 3521
Beniamini, P., & Nakar, E. 2019, *MNRAS*, **482**, 5430
Bernardini, M. G., Margutti, R., Chincarini, G., Guidorzi, C., & Mao, J. 2011, *A&A*, **526**, A27
Burrows, D. N., Romano, P., Falcone, A., et al. 2005, *Sci*, **309**, 1833
Cannizzo, J. K., Troja, E., & Gehrels, N. 2011, *ApJ*, **734**, 35
Chincarini, G., Mao, J., Margutti, R., et al. 2010, *MNRAS*, **406**, 2113
Chincarini, G., Moretti, A., Romano, P., et al. 2007, *ApJ*, **671**, 1903
Curran, P. A., Starling, R. L. C., O’Brien, P. T., et al. 2008, *A&A*, **487**, 533
Dainotti, M. G., Bhardwaj, S., Cook, C., et al. 2024, *ApJS*, **277**, 31

- Dainotti, M. G., Nagataki, S., Maeda, K., Postnikov, S., & Pian, E. 2017, *A&A*, **600**, A98
- Dainotti, M. G., Sharma, R., Narendra, A., et al. 2023, *ApJS*, **267**, 42
- Dainotti, M. G., Willingale, R., Capozziello, S., Fabrizio Cardone, V., & Ostrowski, M. 2010, *ApJL*, **722**, L215
- Dall’Osso, S., Stratta, G., Guetta, D., et al. 2011, *A&A*, **526**, A121
- Dereli-Bégué, H., Pe’er, A., Ryde, F., et al. 2022, *NatCo*, **13**, 5611
- Duque, R., Beniamini, P., Daigne, F., & Mochkovitch, R. 2022, *MNRAS*, **513**, 951
- Eichler, D. 2014, *ApJL*, **787**, L32
- Eichler, D., & Granot, J. 2006, *ApJL*, **641**, L5
- Evans, P. A., Beardmore, A. P., Page, K. L., et al. 2007, *A&A*, **469**, 379
- Evans, P. A., Beardmore, A. P., Page, K. L., et al. 2009, *MNRAS*, **397**, 1177
- Falcone, A. D., Burrows, D. N., Lazzati, D., et al. 2006, *ApJ*, **641**, 1010
- Falcone, A. D., Morris, D., Racusin, J., et al. 2007, *ApJ*, **671**, 1921
- Fan, Y., & Piran, T. 2006, *MNRAS*, **369**, 197
- Fan, Y. Z., & Wei, D. M. 2005, *MNRAS*, **364**, L42
- Fenimore, E. E., Epstein, R. I., & Ho, C. 1993, *A&AS*, **97**, 59
- Feroz, F., Hobson, M. P., & Bridges, M. 2009, *MNRAS*, **398**, 1601
- Gehrels, N., Chincarini, G., Giommi, P., et al. 2004, *ApJ*, **611**, 1005
- Genet, F., Daigne, F., & Mochkovitch, R. 2007, *MNRAS*, **381**, 732
- Giannios, D. 2006, *A&A*, **455**, L5
- Gibson, S. L., Wynn, G. A., Gompertz, B. P., & O’Brien, P. T. 2018, *MNRAS*, **478**, 4323
- Granot, J., Königl, A., & Piran, T. 2006, *MNRAS*, **370**, 1946
- Granot, J., & Kumar, P. 2006, *MNRAS*, **366**, L13
- Granot, J., & Sari, R. 2002, *ApJ*, **568**, 820
- Grupe, D., Gronwall, C., Wang, X.-Y., et al. 2007, *ApJ*, **662**, 443
- Hascoët, R., Daigne, F., & Mochkovitch, R. 2014, *MNRAS*, **442**, 20
- Hinshaw, G., Weiland, J. L., Hill, R. S., et al. 2009, *ApJS*, **180**, 225
- Ioka, K., Kobayashi, S., & Zhang, B. 2005, *ApJ*, **631**, 429
- Kocevski, D., & Petrosian, V. 2013, *ApJ*, **765**, 116
- Krolik, J. H., & Pier, E. A. 1991, *ApJ*, **373**, 277
- Kumar, P., Narayan, R., & Johnson, J. L. 2008a, *MNRAS*, **388**, 1729
- Kumar, P., Narayan, R., & Johnson, J. L. 2008b, *Sci*, **321**, 376
- Kumar, P., & Zhang, B. 2015, *PhR*, **561**, 1
- Lazzati, D., Blackwell, C. H., Morsony, B. J., & Begelman, M. C. 2011, *MNRAS*, **411**, L16
- Lazzati, D., & Perna, R. 2007, *MNRAS*, **375**, L46
- Lenart, A. L., Dainotti, M. G., Khatiya, N., et al. 2025, *JHEAp*, **13**, 61
- Li, L., Wu, X.-F., Lei, W.-H., et al. 2018, *ApJS*, **236**, 26
- Margutti, R., Bernardini, G., Barniol Duran, R., et al. 2011, *MNRAS*, **410**, 1064
- Mészáros, P. 2006, *RPPh*, **69**, 2259
- Mészáros, P., & Rees, M. J. 1993, *ApJ*, **405**, 278
- Mészáros, P., & Rees, M. J. 1997, *ApJ*, **476**, 232
- Mészáros, P., Rees, M. J., & Wijers, R. A. M. J. 1998, *ApJ*, **499**, 301
- Metzger, B. D., Giannios, D., Thompson, T. A., Bucciantini, N., & Quataert, E. 2011, *MNRAS*, **413**, 2031
- Narendra, A., Dainotti, M., Sarkar, M., et al. 2024, arXiv:2410.13985
- Norris, J. P., Bonnell, J. T., Kazanas, D., et al. 2005, *ApJ*, **627**, 324
- Nousek, J. A., Kouveliotou, C., Grupe, D., et al. 2006, *ApJ*, **642**, 389
- O’Brien, P. T., Willingale, R., Osborne, J., et al. 2006, *ApJ*, **647**, 1213
- Oganesyan, G., Ascenzi, S., Branchesi, M., et al. 2020, *ApJ*, **893**, 88
- Panaiteescu, A., & Kumar, P. 2001, *ApJL*, **560**, L49
- Panaiteescu, A., & Kumar, P. 2002, *ApJ*, **571**, 779
- Perri, M., Guetta, D., Antonelli, L. A., et al. 2007, *A&A*, **471**, 83
- Piran, T. 2004, *RvMP*, **76**, 1143
- Racusin, J. L., Karpov, S. V., Sokolowski, M., et al. 2008, *Natur*, **455**, 183
- Racusin, J. L., Oates, S. R., Schady, P., et al. 2011, *ApJ*, **738**, 138
- Rea, N., Gullón, M., Pons, J. A., et al. 2015, *ApJ*, **813**, 92
- Rees, M. J., & Mészáros, P. 1992, *MNRAS*, **258**, 41P
- Ronchini, S., Stratta, G., Rossi, A., et al. 2023, *A&A*, **675**, A117
- Ronchini, S., Oganesyan, G., Branchesi, M., et al. 2021, *NatCo*, **12**, 4040
- Rowlinson, A., Gompertz, B. P., Dainotti, M., et al. 2014, *MNRAS*, **443**, 1779
- Saji, J., Iyyani, S., & Mazde, K. 2023, *ApJS*, **269**, 2
- Sari, R., Piran, T., & Narayan, R. 1998, *ApJL*, **497**, L17
- Shen, R., & Matzner, C. D. 2012, *ApJ*, **744**, 36
- Srinivasaragavan, G. P., Dainotti, M. G., Fraija, N., et al. 2020, *ApJ*, **903**, 18
- Stratta, G., Dainotti, M. G., Dall’Osso, S., Hernandez, X., & De Cesare, G. 2018, *ApJ*, **869**, 155
- Tagliaferri, G., Goad, M., Chincarini, G., et al. 2005, *Natur*, **436**, 985
- Toma, K., Ioka, K., Yamazaki, R., & Nakamura, T. 2006, *ApJL*, **640**, L139
- Uhm, Z. L., & Beloborodov, A. M. 2007, *ApJL*, **665**, L93
- van Eerten, H. 2014, *MNRAS*, **442**, 3495
- van Eerten, H. J. 2014, *MNRAS*, **445**, 2414
- Willingale, R., O’Brien, P. T., Osborne, J. P., et al. 2007, *ApJ*, **662**, 1093
- Yi, S.-X., Du, M., & Liu, T. 2022, *ApJ*, **924**, 69
- Yi, S.-X., Xi, S.-Q., Yu, H., et al. 2016, *ApJS*, **224**, 20
- Yost, S. A., Harrison, F. A., Sari, R., & Frail, D. A. 2003, *ApJ*, **597**, 459
- Zhang, B., Fan, Y. Z., Dyks, J., et al. 2006, *ApJ*, **642**, 354